



## From classical thermodynamics to phase-field method

Long-Qing Chen<sup>a</sup>, Yuhong Zhao<sup>b</sup>

<sup>a</sup> Department of Materials Science and Engineering and Materials Research Institute, The Pennsylvania State University, PA 16803, USA

<sup>b</sup> School of Materials Science and Engineering, North University of China, Taiyuan 030051, China



### ARTICLE INFO

**Keywords:**

Phase-field method  
First law of thermodynamics  
Second law of thermodynamics  
Classical thermodynamics  
Microstructure  
Mesoscale

### ABSTRACT

Phase-field method is a density-based computational method at the mesoscale for modeling and predicting the temporal microstructure and property evolution during materials processes. The focus of this article is on connecting the most common phase-field equations to the very basic first and second laws of classical thermodynamics through rudimentary irreversible thermodynamics. It briefly discusses the relations of the continuum phase-field equations to their counter parts at the microscopic and atomic levels. It attempts to clarify the contributions of long-range elastic, electrostatic, and magnetic interactions to domain structure evolution during structural, ferroelectric, and ferromagnetic phase transformations by separating order parameter changes due to the presence of quasi-static fields and those arising from phase transformations. A few examples are presented to demonstrate the possibility of employing the phase-field method to provide guidance to designing materials for optimum properties or discovering novel mesoscale phenomena or new materials functionalities. The article ends with a brief perspective on a number of potential future directions on the development and applications of phase-field method beyond its traditional applications to structural alloys.

### 1. Introduction

Phase-field method is a mesoscale computational technique for modeling and predicting spatial and temporal evolution of materials microstructures/domain patterns as well as their responses to external fields and thus properties. It is based on the continuum mass density functional theory that can be traced back to the diffuse-interface description of fluid interfaces using the mass density distribution by J.D. van der Waals [1,2]. The term “phase-field” was originally coined for the artificial field introduced to distinguish a solid and a liquid to avoid the tracking of interfaces in a solidification modeling [3–6]. However, it is the generalization of the artificial phase-field to other physical fields representing the spatial distributions of order such as long-range atomic order, compositions of chemical substances, local lattice displacements (or strain), ferroic (ferroelectric, ferromagnetic, ferroelastic) order, etc., that led to the widespread applications of the phase-field method to modeling and predicting the mesoscale microstructural pattern evolution in a wide variety of materials processes. Phase-field method is natural for modeling nanoscale microstructures in thin films and other nanoscale materials systems in which the feature size of microstructural domains is within 1–2 orders of that of typical interfacial width. It automatically takes into account of interfacial contributions to the thermodynamics and evolution of microstructures. It is also possible to incorporate the influence of long-range electrostatic, magnetic, and elastic interactions within a mesoscale microstructure. While early applications are largely focused on solidification [7–17], it has since been applied to numerous other processes such as grain growth [18–21], particle coarsening [22,23], solid state phase transformations [24–29], ferroelectric phase transitions

E-mail addresses: [lqc3@psu.edu](mailto:lqc3@psu.edu) (L.-Q. Chen), [zhaoyuhong@nuc.edu.cn](mailto:zhaoyuhong@nuc.edu.cn) (Y. Zhao).

and domain formation [30–35], electrochemical processes [36–39], as well as mechanical deformation such as dislocation motion [40–42], twinning [43,44], and fracture [45–52]. The same set of phase-field equations have also been employed in modeling biological cells [53–56], topological optimization [57], and image processing [58–61].

Phase-field method has now been established as a mainstream approach among computational materials methods which include density function theory (DFT) calculations, molecular dynamics simulations, Monte Carlo techniques, and macroscopic modeling based on materials constitutive relations. Molecular dynamics simulations of atoms, ions, and molecules or Monte-Carlo simulations of atomic/magnetic/electric configurations are particle-based, which sample or generate instantaneous particle/dipole configurations and then perform statistical averaging over those configurations to obtain macroscopic properties. On the other hand, phase-field method is a density-based approach at the domain and phase microstructure level, similar to the electron density functional theory at the electron level and the atomic density functional theory at the atom level, and hence the stability of a mesoscale microstructure is described by an energy or a free energy functional of one or more density functions or phase-fields describing a microstructure. Atomistic molecular dynamics simulations temporarily discretize the Newton's equations of motion of atoms with time steps of a fraction of the typical lattice vibration period of a crystalline solid, and thus they can be employed to capture the dynamics of lattice vibrations but with typical simulation duration times on the order of picoseconds. In the contrast, phase-field method solves only the phase-field evolution equations describing the slowest evolving fields describing the microstructures and assuming quasi-equilibrium for the fields with much shorter relaxation times. The faster processes are only implicitly taken into account in the thermodynamic energy density functions and in the kinetic coefficients in the evolution equations of a phase-field model. Spatially, phase-field method cannot resolve spatial phenomena smaller than the discretization volume element. In principle, phase-field simulations can be formulated at different spatial and time scales for the same microstructure evolution process just like different experimental microscopic techniques can be used to obtain microstructure images at different spatial resolutions. For example, the typical interfacial width of majority of the surfaces and interfaces in solids are on the order of a couple of nanometers, and hence if one is to spatially resolve the physical order parameter profiles across a solid interface in the phase-field model, the system size is limited to the order of microns even with the use of advanced numerical techniques such as adaptive grid method. One can formulate a phase-field model with a spatial discretization grid much wider than the physical interface, and thus the physical order parameter profile is smeared out over several discretization grids. In general, a larger spatial scale described by a coarser grid also allows larger time steps in numerical solutions and thus longer simulation durations. However, in such cases, the model will have to be formulated in such a way that the smearing of the interface over a distance much larger than its physical width does not quantitatively change the interfacial kinetics.

There exist numerous review articles on the general aspects of phase-field method [62–69]. There have also been review articles on the specific applications of phase-field method, such as solidification [17,70], solid state phase transformations [71–73], ferroelectrics [74,75], deformation and fracture [51,76], nucleation [77], irradiation damage [78–80], electrochemical energy storage [81], two-dimensional materials [82], and fluid flow [83–85].

Therefore, the main objective of this article is not to provide a review of the important advances in the development and applications of phase-field method. Instead, it focuses discussing the fundamental thermodynamic basis for the evolution equations in the phase-field method by utilizing the first and second laws of classical thermodynamics in combination with basic irreversible thermodynamics. It attempts to make a connection between the continuum version of the phase-field method and other well-known density-based approaches such as phase-field crystal [86,87] based on the atomic density functional theory and the microscopic diffusion equations [22,88–90]. The existing applications of the phase-field method have largely been focused on illustrating its capability of modeling materials microstructure evolution phenomena using idealized model systems, testing analytical theories, and helping understand and interpret experimental observations. Therefore, the present article presents a few examples with the main goal to illustrate the possibility of employing the phase-field method to predict, discover, and design mesoscale structures that may potentially possess novel or dramatically enhanced properties. It also briefly discusses possible applications of the phase-field method to modeling a number of materials processes beyond existing applications, including coupled electronic and structural phase transitions in quantum materials, dynamics of mesoscale structure evolution under fast stimuli, microstructure optimization and design through a combination of high throughput generation of microstructures and machine learning.

## 2. From first and second laws of thermodynamics to phase-field method

The thermodynamic basis of the phase-field method was first discussed about 30 years ago by Penrose and Fife [91] and Wang et al [92] starting from an entropy functional of a system going through a phase transition with a particular emphasis on the freezing of a pure liquid. Fried and Gurtin [93,94] proposed a general framework for deriving the phase-field equations, i.e., the Cahn-Hilliard [95] and Allen-Cahn equations [96], by introducing the concept of a generalized micro-forces and employing a mechanical version of the second law of thermodynamics. Here in this article, we discuss the fundamental thermodynamic and kinetic principles underlying the phase-field method starting from the first and second laws of class thermodynamics in combination of basic irreversible thermodynamics in the energy density representation. We believe such a classical thermodynamic framework is more accessible to the large portion of the materials community whose main thermodynamics training is in the realm of classical chemical thermodynamics with some exposure to irreversible thermodynamics.

### 2.1. Definition of variables

We begin the discussion by distinguishing a number of thermodynamic quantities and processes. The thermodynamic quantities of the first type are the thermodynamic properties of a homogeneous system or of materials within a volume element in an inhomogeneous

geneous system:

- Density of matter or amount of matter per unit volume, including entropy density  $s$ , mechanical strain  $\epsilon_{ij}$ , density of chemical species  $c_i$  in unit of number of moles per unit volume, electric displacement  $D_i$ , magnetic induction  $B_i$ , charge density  $\rho_i$ , and density of interfacial areas  $A_v$ .
- Potentials such as temperature  $T$ , pressure  $p$ , chemical potential  $\mu_i$  of chemical species  $i$ , electric potential  $\phi$ , and interfacial energy per unit area  $y$ .

It should be noted for inhomogeneous systems, all the local properties are intensive properties: both the quantities characterizing the densities of different types of matters and the potentials are intensive parameters. The main difference between purely density quantities and potentials is the fact that all the potentials are uniform whereas purely density quantities are different in different regions in a heterogeneous system at equilibrium.

The thermodynamic quantities of the second type are fields: mechanical stress  $\sigma_{ij}$ , electric field  $E_i$ , and magnetic field  $H_i$ , or potential gradients in an inhomogeneous system: temperature gradient  $\nabla T$ , chemical potential gradient  $\nabla \mu_i$ , and electric potential gradient  $\nabla \phi$  ( $= -\vec{E}$ ).

The thermodynamic quantities of the last type are the changes in the thermodynamic properties of a system or a volume element in an inhomogeneous system associated with a thermodynamic process. We use  $ds$ ,  $dc_i$ ,  $d\rho_i$ ,  $dA_v$ ,  $d\epsilon_{ij}$ ,  $dD_i$ ,  $dB_i$ ,  $dT$ ,  $d\mu_i$ ,  $d\sigma_{ij}$ ,  $dE_i$ , and  $dH_i$  to represent their infinitesimal changes. For simplicity of discussion, we ignore the possibility of volume flow, charge flow, and time-dependent magnetic induction, i.e., we will not consider fluid flow and magnetic fields induced by current flows or an electric voltage arising from a time-dependent magnetic induction. We only consider the quasi-static stress, electric, or magnetic fields as a result of a spatial distribution of spontaneous strains, or free charge and electric polarization, or magnetization within a materials microstructure.

## 2.2. Materials processes

To derive kinetic equations including phase-field equations for materials processes, it is also important to distinguish two types of processes. One involves the interactions, e.g., exchange of matter between a homogeneous system and its surroundings or between a volume element and its surrounding elements of an inhomogeneous system, and the other involves internal processes taking place entirely within a system or within a volume element, e.g., transport due to the presence of a potential gradient or chemical reactions and phase transformations driven by local thermodynamic potential reduction at a given location. There are two types of corresponding changes in thermodynamic properties produced by these two kinds of processes:

- The changes in the amount of matter due to reversible matter exchanges ( $ds^e, dc_i^e, d\rho_i^e$ ) between a volume element and its neighboring elements within an inhomogeneous system in a process or the changes in the properties of the system ( $d\epsilon_{ij}^e, dD_i^e, dB_i^e$ ) arising from the presence of quasi-static stress, electric, and magnetic fields.
- The changes in the amount of matter due to internal irreversible processes such as phase transformations, chemical reactions, and microstructure coarsening driven by local thermodynamic potential reduction, or entropy and mass transport driven by local potential gradients. We label the infinitesimal spontaneous changes in entropy density, chemical concentration of species  $i$ , interfacial area density, strain, polarization, and magnetization due to internal processes using  $ds^o$ ,  $dc_i^o$ ,  $dA_v^o$ ,  $d\epsilon_{ij}^o$ ,  $dP_i^o$ , and  $dM_i^o$ , respectively.

## 2.3. First law of thermodynamics

The first law of thermodynamics is about the conservation of energy, so the change in the internal energy density  $du$  of a volume element in an inhomogeneous system is equal to the amount of energy  $du^e$  per unit volume transferred to the volume element from its surrounding elements, i.e.,

$$du = du^e \quad (2.1)$$

We now consider the internal energy density change of a volume element as a result of infinitesimal amounts of transfer in entropy  $ds^e$ , chemical species  $dc_i^e$ , and charge  $d\rho_i^e$  from the neighboring volume elements as well as of the changes in strain  $d\epsilon_{ij}^e$ , electric displacement  $dD_i^e$ , and magnetic induction  $dB_i^e$  due to the presence of stress  $\sigma_{ij}$ , electric field  $E_i$ , and magnetic field  $H_i$ :

$$du^e = Tds^e + \mu_i dc_i^e + \phi d\rho_i^e + \sigma_{ij} d\epsilon_{ij}^e + E_i dD_i^e + H_i dB_i^e \quad (2.2)$$

The last three terms in Eq. (2.2) can also be considered as the mechanical, electric, and magnetic work done on the volume element of interest by the neighboring volume elements. In all the equations in this article, we adopt the Einstein summation convention, i.e., repeating indices in the same term imply summation over those indices. For example, in Eq. (2.2),

$$E_i dD_i^e = E_1 dD_1^e + E_2 dD_2^e + E_3 dD_3^e \quad (2.3)$$

If we combine the chemical potential and electric potential, we can rewrite Eq. (2.2) as

$$du^e = Tds^e + \tilde{\mu}_i dc_i^e + \sigma_{ij} de_{ij}^e + E_i dD_i^e + H_i dB_i^e \quad (2.4)$$

where  $\tilde{\mu}_i = \mu_i + z_i \mathcal{F}\phi$  is the electrochemical potential of species  $i$  with  $\mathcal{F}$  being the Faraday constant and  $z_i$  the valence of species  $i$ .

#### 2.4. Differential form of fundamental equation of thermodynamics

If there are no internal processes taking place within the volume element of interest during the exchange of various forms of matter between a volume element and its surrounding elements, the amounts of matter exchanges between the volume element and its surrounding elements in Eq. (2.2) can be replaced by the changes in the properties of the volume element, i.e.,

$$ds = ds^e, dc_i = dc_i^e, de_{ij} = de_{ij}^e, dD_i = dD_i^e, dB_i = dB_i^e \quad (2.5)$$

Therefore, the change in internal energy of the volume element can be written as

$$du = Tds + \mu_i dc_i + \sigma_{ij} de_{ij} + E_i dD_i + H_i dB_i \quad (2.6)$$

which is the differential form for the fundamental equation of thermodynamics in the energy density representation for a volume element. It describes the relationships among the thermodynamic properties of the volume element at equilibrium states and their variations during reversible processes, and thus this equation is valid for all reversible or quasistatic processes.

#### 2.5. Second law of thermodynamics

Now we consider the possibility of irreversible internal processes such as heat conduction or entropy transport, mass transfer, chemical reactions, and phase transformations. In such processes, the changes in the thermodynamic properties of a volume element come from two types of contributions: (a) changes due to the conservative exchanges of various forms of matter between a volume element and its surrounding elements or changes due to the presence of quasi-static stress, electric, and magnetic fields and (b) changes due to internal spontaneous, irreversible processes.

According to the second law of thermodynamics, the entropy density change  $ds$  for the volume element of interest is the sum of the amount of entropy  $ds^e$  transported to the volume element from its surrounding elements and the amount of entropy  $ds^o$  produced due to the internal processes within the volume element,

$$ds = ds^e + ds^o \quad (2.7)$$

where  $ds^o$  is always greater or equal to zero, i.e.,

$$ds^o \geq 0 \quad (2.8)$$

#### 2.6. Energy dissipation, driving forces, rate of processes

The changes in the concentration  $dc_i$  of chemical species may result from the concentration change  $dc_i^e$  due to the exchanges between a volume element and its neighboring volume elements or the spontaneous change  $dc_i^o$  due to chemical reactions within the volume element,

$$dc_i = dc_i^e + dc_i^o \quad (2.9)$$

The amount of concentration change  $dc_i^o$  can be positive or negative depending on whether the species  $i$  is a reactant or a product in a reaction. Similarly, the changes in strain  $de_{ij}$ , electric displacement  $dD_i$ , and magnetic induction  $dB_i$  may come from changes  $de_{ij}^e$ ,  $dD_i^e$ , and  $dB_i^e$  due to the presence of quasi-static stress, electric, and magnetic fields within the volume element or the spontaneous changes  $de_{ij}^o$ ,  $dP_i^o$ , and  $dM_i^o$  arising from structural, ferroelectric, and ferromagnetic phase transitions within the volume element,

$$de_{ij} = de_{ij}^e + de_{ij}^o \quad (2.10)$$

$$dD_i = dD_i^e + dP_i^o \quad (2.11)$$

$$dB_i = dB_i^e + dM_i^o \quad (2.12)$$

Now let us consider the rates of change in the thermodynamic properties per unit volume within a volume element. The change rate of local entropy density within a volume element is the sum of the net entropy flux  $-\nabla \cdot \vec{J}_s$  into the volume element, or the negative of the divergence of entropy flux  $\vec{J}_s$ , and the rate of internal entropy production  $ds^o/dt$  within the volume element, i.e.,

$$T \frac{ds}{dt} = -T \nabla \cdot \vec{J}_s + T \frac{ds^o}{dt} = -\nabla \cdot \left( T \vec{J}_s \right) + \nabla T \cdot \vec{J}_s + T \frac{ds^o}{dt} \quad (2.13)$$

where  $-\nabla \cdot \left( T \vec{J}_s \right)$  is the net thermal energy per unit volume transferred into the volume element.

Similarly, the rate of local chemical concentration change arises from the exchanges between the volume element and its surrounding elements and chemical reactions within the volume element,

$$\mu_i \frac{dc_i}{dt} = -\mu_i \nabla \cdot \vec{J}_i + \mu_i \frac{dc_i^o}{dt} = -\nabla \cdot (\mu_i \vec{J}_i) + \nabla \mu_i \cdot \vec{J}_i + \mu_i \frac{dc_i^o}{dt} \quad (2.14)$$

where  $-\nabla \cdot \vec{J}_i$  is the net flux of chemical species from the neighboring volume elements into the volume element,  $-\nabla \cdot (\mu_i \vec{J}_i)$  is the net electrochemical energy density transferred into the volume element, and  $dc_i^o/dt$  is the rate of concentration change of chemical species  $i$  due to chemical reactions within the volume element. It should be emphasized that here we will treat all the concentrations  $c_i$  as mutually independent, and the flux  $\vec{J}_i$  describes the rates of transport of species  $i$  in a media, and thus they are also all independent. However, if it is a multicomponent solution with a fixed overall concentration  $c = c_1 + c_2 + \dots + c_n$ , there are only  $n-1$  independent concentrations and thus  $n-1$  independent fluxes.

The rates of change in the local strain, electric displacement, and magnetic flux density can be due to either the presence of quasi-static local stress, electric, and magnetic fields or the structural, ferroelectric, and ferromagnetic phase transitions within the volume element,

$$\sigma_{ij} \frac{d\varepsilon_{ij}}{dt} = \sigma_{ij} \frac{d\varepsilon_{ij}^e}{dt} - A_e \frac{d\varepsilon_{ij}^o}{dt} \quad (2.15)$$

$$E_i \frac{dD_i}{dt} = E_i \frac{dD_i^e}{dt} - A_p \frac{dP_i^o}{dt} \quad (2.16)$$

$$H_i \frac{dB_i}{dt} = H_i \frac{dB_i^e}{dt} - A_M \frac{dM_i^o}{dt} \quad (2.17)$$

where  $\sigma_{ij} d\varepsilon_{ij}^e/dt$ ,  $E_i dD_i^e/dt$ , and  $H_i dB_i^e/dt$  are the rates of mechanical, electric, and magnetic work done on the volume element by the surrounding elements, and  $A_e$ ,  $A_p$ , and  $A_M$  are the thermodynamic driving forces for the structural, ferroelectric, and ferromagnetic phase transitions. It should be noted that for simplicity of discussion, the possible flows of volume, strain, polarization, and magnetization due to gradients in pressure, stress, electric field, and magnetic field are not considered.

By adding left-hand sides of equations from Eqs. (2.13)–(2.17), we have

$$\frac{du}{dt} = \frac{du^e}{dt} = T \frac{ds}{dt} + \mu_i \frac{dc_i}{dt} + \sigma_{ij} \frac{d\varepsilon_{ij}}{dt} + E_i \frac{dD_i}{dt} + H_i \frac{dB_i}{dt} \quad (2.18)$$

The sum of the right-hand sides of Eqs. (2.13)–(2.17) is

$$\frac{du}{dt} = \frac{du^e}{dt} = -\nabla \cdot (T \vec{J}_s) + \nabla T \cdot \vec{J}_s + T \frac{ds^o}{dt} - \nabla \cdot (\mu_i \vec{J}_i) + \nabla \mu_i \cdot \vec{J}_i + \mu_i \frac{dc_i^o}{dt} + \sigma_{ij} \frac{d\varepsilon_{ij}^e}{dt} - A_e \frac{d\varepsilon_{ij}^o}{dt} + E_i \frac{dD_i^e}{dt} - A_p \frac{dP_i^o}{dt} + H_i \frac{dB_i^e}{dt} - A_M \frac{dM_i^o}{dt} \quad (2.19)$$

From energy conservation according to the first law of thermodynamics, we have

$$\frac{du}{dt} = \frac{du^e}{dt} = -\nabla \cdot (T \vec{J}_s) - \nabla \cdot (\mu_i \vec{J}_i) + \sigma_{ij} \frac{d\varepsilon_{ij}^e}{dt} + E_i \frac{dD_i^e}{dt} + H_i \frac{dB_i^e}{dt} \quad (2.20)$$

which shows that the rate of internal energy change of a volume element is equal to the sum of exchanges in thermal and electrochemical energy as well as in mechanical, electric, and magnetic work between the volume element and its neighboring elements.

Taking into account Eq. (2.20), we can rewrite Eq. (2.19) as

$$T \frac{ds^o}{dt} = -\nabla T \cdot \vec{J}_s - \nabla \mu_i \cdot \vec{J}_i + A_r \frac{d\xi_r}{dt} + A_e \frac{d\varepsilon_{ij}^o}{dt} + A_p \frac{dP_i^o}{dt} + A_M \frac{dM_i^o}{dt} \quad (2.21)$$

where we have rewritten the chemical reaction term in Eq. (2.19) in terms of the extent  $\xi_r$ , rate  $d\xi_r/dt$  per unit volume, and driving force  $A_r$  of the  $r^{\text{th}}$  chemical reaction. Eq. (2.21) represents the rate of energy dissipation or conversion of useful energy to thermal energy during irreversible internal processes including entropy transport, mass transfer, chemical reactions, as well as structural, ferroelectric, and ferromagnetic phase transitions.

Additional possible internal processes such as solidification, melting, as well as reduction in internal interfacial area density such as grain growth, domain coarsening, and Ostwald ripening may simultaneously take place and contribute to the entropy production. Therefore, we rewrite a general version of Eq. (2.21) for the rate of thermal energy production,

$$T \frac{ds^o}{dt} = -\nabla T \cdot \vec{J}_s - \nabla \mu_i \cdot \vec{J}_i + A_i \frac{d\xi_i}{dt} \quad (2.22)$$

where  $-\nabla T$ ,  $-\nabla \mu_i$ , and  $A_i$  represent thermodynamic driving forces for entropy transport, electrochemical mass transport, and other internal processes, respectively while  $\vec{J}_s$ ,  $\vec{J}_i$ , and  $d\xi_i/dt$  are the corresponding responses representing the entropy flux density, mass

flux density of chemical species  $i$ , and rate of internal process  $i$ , respectively.

The first term of the right-hand side of Eq. (2.22) represents the rate of thermal energy production per unit volume due to entropy transport, the second term is the amount of thermal energy produced per unit volume due to the mass transfer, and the last term sums up the thermal energy production from all other possible internal processes, i.e.,

$$A_i \frac{d\xi_i}{dt} = A_r \frac{d\xi_r}{dt} + A_e \frac{d\epsilon_{ij}^o}{dt} + A_P \frac{dP_i^o}{dt} + A_M \frac{dM_i^o}{dt} - \gamma \frac{dA_v}{dt} + \dots \quad (2.23)$$

where  $dA_v/dt$  is the rate of change in the area density of the internal interfaces, and  $\gamma$  is the interfacial energy per unit area of the interfaces.

The amount of internal energy dissipated as thermal energy per unit volume at constant entropy density is given by

$$\frac{du^o}{dt} = -T \frac{ds^o}{dt} = \nabla T \cdot \vec{J}_s + \nabla \mu_i \cdot \vec{J}_i - A_i \frac{d\xi_i}{dt} \quad (2.24)$$

The total rate of change of internal energy density including both reversible and irreversible processes is

$$\frac{du}{dt} = T \frac{ds}{dt} + \mu_i \frac{d(c_i - c_i^o)}{dt} + \sigma_{ij} \frac{d(\epsilon_{ij} - \epsilon_{ij}^o)}{dt} + E_i \frac{d(D_i - P_i^o)}{dt} + H_i \frac{d(B_i - M_i^o)}{dt} + \nabla T \cdot \vec{J}_s + \nabla \mu_i \cdot \vec{J}_i - A_i \frac{d\xi_i}{dt} \quad (2.25)$$

## 2.7. Fundamental equations of thermodynamics incorporating process order parameters

Now we can establish the thermodynamic energy density functions that we employ in the phase-field method as a function of thermodynamic variables as well as order parameters or phase fields. From Eq. (2.25), we can deduce that the internal energy density can be expressed as

$$u = u(s, c_i, \epsilon_{ij}, D_i, B_i, \xi_i) \quad (2.26)$$

where  $u$  and  $s$  are the internal energy density and entropy density of a volume element, respectively, and  $\xi_i$  is an order parameter such as spontaneous strain  $\epsilon_{ij}^o$ , spontaneous electric polarization  $P_i^o$ , or spontaneous magnetization  $M_i^o$ , or a phase field characterizing the extent of an internal process such as solidification, order-disorder transition, chemical reaction, microstructural coarsening, etc.

Since most of the phase-field simulations are performed at constant temperature, we often employ Helmholtz free energy density to represent the thermodynamics of a system,

$$f = u - Ts = f(T, c_i, \epsilon_{ij}, D_i, B_i, \xi_i) \quad (2.27)$$

The total rate of change in the Helmholtz free energy density within the volume element including both reversible and irreversible processes is

$$\frac{df}{dt} = -s \frac{dT}{dt} + \mu_i \frac{d(c_i - c_i^o)}{dt} + \sigma_{ij} \frac{d(\epsilon_{ij} - \epsilon_{ij}^o)}{dt} + E_i \frac{d(D_i - P_i^o)}{dt} + H_i \frac{d(B_i - M_i^o)}{dt} + \nabla T \cdot \vec{J}_s + \nabla \mu_i \cdot \vec{J}_i - A_i \frac{d\xi_i}{dt} \quad (2.28)$$

where the thermodynamic driving force for a given internal process  $\xi_i$  is given by

$$A_i = - \left( \frac{\partial f}{\partial \xi_i} \right)_{T, c_i, \epsilon_{ij}, D_i, B_i, \xi_j \neq i} \geq 0 \quad (2.29)$$

At constant uniform temperature, the rate of thermal energy production and thus the Helmholtz free energy dissipation rate is given by

$$\frac{df^o}{dt} = -T \frac{ds^o}{dt} = \nabla \mu_i \cdot \vec{J}_{c_i} - A_i \frac{d\xi_i}{dt} \quad (2.30)$$

Other forms of the fundamental equation can be obtained by Legendre transforms, e.g., the Gibbs free energy density,

$$g = u - Ts - \sigma_{ij} \epsilon_{ij} - E_i D_i - H_i B_i = g(T, c_i, \sigma_{ij}, E_i, H_i, \xi_i) \quad (2.31)$$

The parameter  $\xi_i$  measures the extent of an internal process with

$$\xi_i = \begin{cases} \xi_i^o & \text{or } 0 \text{ at the start of the process} \\ \xi_i^{eq} & \text{at the end of the process} \end{cases} \quad (2.32)$$

In the phase-field method, all the parameters  $\xi_i$  except the interfacial area density  $A_v$  in Eq. (2.23) are regarded as order parameters or phase-fields. For example, in a phase-field model of a phase transformation from phase  $\alpha$  to  $\beta$ ,

$$\alpha \rightarrow \beta, \quad (2.33)$$

the driving force for the transformation is

$$A = \mu_\alpha - \mu_\beta \quad (2.34)$$

where  $\mu_\alpha$  and  $\mu_\beta$  are the chemical potentials of  $\alpha$  and  $\beta$  phases, respectively. The magnitude of internal process parameter or order parameter indicates the degree of completion for the phase transformation, e.g.,

$$\begin{cases} \xi_i = 0 & \text{represents 100\% of the original, parent phase } \alpha \\ 0 < \xi_i < 1 & \text{represents a mixture of parent } \alpha \text{ and new } \beta \text{ phases} \\ \xi_i^{eq} = 1 & \text{represents 100\% of the transformed, new phase} \end{cases} \quad (2.35)$$

The variation of Helmholtz free energy density during the transformation is given by

$$\frac{df}{dt} = -T \frac{ds^o}{dt} = -A \frac{d\xi}{dt} \quad (2.36)$$

Similarly, for a general chemical reaction,



the driving force for the reaction is

$$A = \sum_i \nu_{B_i} \mu_{B_i} - \sum_j \nu_{C_j} \mu_{C_j} \quad (2.38)$$

where  $\mu_{B_i}$  and  $\mu_{C_j}$  are the chemical potentials of reacting species  $B_i$  and product species  $C_j$ , respectively. The magnitude of the internal process parameter  $\xi_r$  describes the degree of completion for the reaction. For example,

$$\begin{cases} \xi_r = 0 & \text{represents 100\% of the reacting species} \\ 0 < \xi_r < 1 & \text{represents a mixture of reacting and product species} \\ \xi_r^{eq} = 1 & \text{represents 100\% of the product species} \end{cases} \quad (2.39)$$

The rate of change of Helmholtz free energy density during the chemical reaction is given by

$$\frac{df}{dt} = -T \frac{ds^o}{dt} = -A_r \frac{d\xi_r}{dt} \quad (2.40)$$

As a final example in this section, let us consider a ferroelectric phase transition in a ferroelectric crystal with a homogeneous composition. The phase field  $\xi_i$  in this case is the spontaneous polarization  $P_i^o$ , and the driving force for a ferroelectric phase transition of such a crystal is a nonlinear function of  $P_i^o$ . Ignoring any other secondary thermodynamic order parameters such as strain, we can write down the differential form for the Helmholtz free energy density  $f$  of a ferroelectric crystal,

$$df = -sdT + E_i dD_i^e - A_i dP_i^o = -sdT + E_i d(D_i - P_i^o) - A_i dP_i^o \quad (2.41)$$

Assuming a linear relation between the electric field and electric displacement, we can write the Helmholtz free energy density as a function of order parameter  $P_i^o$  as

$$f(T, D_i, P_i^o) = \frac{1}{2} E_i (D_i - P_i^o) + f_o(T, P_i^o = 0) + \Delta f(T, P_i^o) \quad (2.42)$$

where the first term on the right-hand side is the electrostatic energy,  $f_o(T, P_i^o = 0)$  is the Helmholtz free energy of the initial nonequilibrium state with zero spontaneous polarization, and  $\Delta f(T, P_i^o)$  is the amount of energy dissipated during the process of the spontaneous polarization of the crystal changing from 0 to  $P_i^o$ . In the thermodynamic description of ferroelectric crystals,  $\Delta f(T, P_i^o)$  is typically expressed in terms of a polynomial based on the Landau free energy density function [97], e.g.,

$$\begin{aligned} \Delta f(T, P_i^o) = & a_o(T - T_c) \left[ (P_1^o)^2 + (P_2^o)^2 + (P_3^o)^2 \right] + a_{11} \left[ (P_1^o)^4 + (P_2^o)^4 + (P_3^o)^4 \right] + a_{12} \left[ (P_1^o)^2 (P_2^o)^2 + (P_2^o)^2 (P_3^o)^2 + (P_1^o)^2 (P_3^o)^2 \right] \\ & + a_{123} (P_1^o)^2 (P_2^o)^2 (P_3^o)^2 \end{aligned}$$

where  $T_c$  is the critical temperature for the ferroelectric phase transition, and  $a_o$ ,  $a_{11}$ ,  $a_{12}$ , and  $a_{123}$  are constants related to linear and nonlinear ferroelectric properties. In this case, the driving force per unit volume is given by

$$A(T, P_i^o) = - \left[ \frac{\partial \Delta f(P_i^o)}{\partial P_i^o} \right]_T \quad (2.43)$$

which is generally a highly nonlinear function of  $P_i^o$ .

The rate of variation of Helmholtz free energy density during a ferroelectric phase transition is given by

$$\frac{df}{dt} = -T \frac{ds^o}{dt} = -A(T, P_i^o) \frac{dP_i^o}{dt} = \left[ \frac{\partial \Delta f(T, P_i^o)}{\partial P_i^o} \right]_{T,V} \frac{dP_i^o}{dt} \quad (2.44)$$

As discussed above, the internal process can be very general. It can be a structural phase transformation, a compositional phase separation, a chemical reaction, an electronic phase transition, etc. In principle, any process can be characterized by physically well-defined order parameters or phase fields that distinguish the initial states and final states. For example, an order parameter is zero in the high-temperature disordered phase and has a finite value in the low-temperature ordered phase in a disorder–order phase transition. Some examples relating the extent of an internal process to an order parameter in the phase-field method and the corresponding thermodynamic driving force for the process are summarized in [Table 1](#).

### 3. Isothermal relaxation of a nonequilibrium homogeneous state

Before we discuss phase-field equations for inhomogeneous systems, it is instructional to first consider a simple homogeneous system to connect thermodynamic driving forces to the kinetics of a process. A process taking place homogeneously in a system or a process taking place at a given point of an inhomogeneous system is a non-conserved process. A quantitative description of the kinetics of a process requires two pieces of information: one is the thermodynamic driving force for the process determined entirely by thermodynamics, and the other is the kinetic rate constant which is related to the energy barrier that the process has to overcome. After we identify the driving forces for internal processes in a system, we can formulate a kinetic theory to describe their temporal evolution.

As a model illustrative example, let us consider an initially thermodynamically unstable homogeneous state going through an internal process without creating any interfaces. The amount of change in the Helmholtz free energy density with respect to the order parameter describing the degree of completion of the process is given by

$$df = -Ad\xi \quad (3.1)$$

If the driving force  $A$  is small, the kinetics can be approximated by a linear relation between the rate of the process and its driving force, i.e.

$$\frac{d\xi}{dt} \propto A = -\frac{\partial f}{\partial \xi} \quad (3.2)$$

If we use  $L_\xi$  to represent the linear kinetic coefficient, we have

$$\frac{d\xi}{dt} = L_\xi A = -L_\xi \frac{\partial f}{\partial \xi} \quad (3.3)$$

The rate of energy dissipation per unit volume is then given by

$$\frac{\partial f}{\partial t} = -\frac{Ad\xi}{dt} = -L_\xi A^2 \quad (3.4)$$

The corresponding rate of entropy production per unit volume is given by

$$\frac{ds^o}{dt} = \frac{L_\xi A^2}{T} \quad (3.5)$$

If the initial state is unstable, the second derivative of  $f$  with respect to  $\xi$  is negative near  $\xi = 0$ , and there is no barrier to overcome for the process. Let us approximate the Helmholtz free energy density at small  $\xi$  as a parabola,

**Table 1**

Relating the extent of an internal process to a phase-field order parameter and the corresponding driving forces for a number of well-known processes in materials.

$\xi_i$	Order Parameter	$A_i = -\frac{\partial f}{\partial \xi_i}$	Process
$\xi$	Extent of reaction	$\frac{\partial f}{\partial \xi} = \nu_{B_1}\mu_{B_1} - \nu_{C_1}\mu_{C_1}$	Chemical Reaction $\nu_{B_1}B_1 + \nu_{B_2}B_2 + \dots \rightarrow \nu_{C_1}C_1 + \nu_{C_2}C_2 + \dots$
$\eta$	Phase-field	$\frac{\partial f}{\partial \eta} = \mu_\alpha - \mu_\beta$	Order-disorder, solidification, etc. $\alpha \rightarrow \beta$
$\epsilon_{ij}^o$	Strain	$\frac{\partial f}{\partial \epsilon_{ij}^o}$	Ferroelastic transition
$P_i^o$	Electric polarization	$\frac{\partial f}{\partial P_i^o}$	Ferroelectric transition
$M_i^o$	Magnetization	$\frac{\partial f}{\partial M_i^o}$	Ferromagnetic transition
$\theta_i$	Oxygen octahedral tilt	$\frac{\partial f}{\partial \theta_i}$	Ferrodistortive transition in oxides
$\varphi_i$	Electronic order parameter	$\frac{\partial f}{\partial \varphi_i}$	Metal-Insulator Transition
$\psi$	Superconducting order parameter	$\frac{\partial f}{\partial \psi^*}$	Superconducting phase transition

$$f(\xi) = -\frac{a}{2}\xi^2 \quad (3.6)$$

where  $a$  is a positive constant. The rate of the process is simplified to

$$\frac{d\xi}{dt} = -L_\xi \frac{\partial f}{\partial \xi} = L_\xi a \xi \quad (3.7)$$

Integrating both sides of Eq. (3.7), we have

$$\int \frac{d\xi}{\xi} = \int L_\xi a dt \quad (3.8)$$

Assuming  $L_\xi$  is a constant independent of  $\xi$  and  $t$ , we can easily solve the above ordinary differential equation. However, it is interesting to notice that if the initial value of  $\xi$  is exactly zero, the amount of time to accomplish the process will be infinite, i.e.,

$$t = \frac{1}{L_\xi a} \ln \frac{\xi}{0} \rightarrow \infty \quad (3.9)$$

Therefore, it is necessary to have a very small perturbation or fluctuation to initiate the process since the driving force  $D = -\partial f / \partial \xi = 0$  at  $\xi = 0$ . This is the very same reason that in phase-field simulations, small fluctuations have to be introduced in an initially homogeneous state, even if the initial state is thermodynamically unstable, to initiate the temporal evolution process. For an initially small  $\xi_0$ ,

$$\ln \frac{\xi}{\xi_0} = L_\xi a t \quad (3.10)$$

which shows that  $\xi$  will grow exponentially as a function of time, i.e.,

$$\xi = \xi_0 e^{L_\xi a t} \quad (3.11)$$

Eq. (3.11) is only valid for very small  $t \ll \tau = 1/L_\xi a$ , where  $\tau$  can be considered as the relaxation time for the internal process since Eq. (3.11) shows that  $\xi$  will grow with time indefinitely. Of course, this unlimited growth is not realistic and is due to the unrealistic free energy expression (3.6). One has to include higher order terms in  $\xi$  in the free energy expression to counterbalance the free energy decrease to eventually reach a metastable or stable state.

Now let us assume that the final equilibrium state has two degenerate states described by  $\xi = 1$  or  $\xi = -1$ , and the dependence of Helmholtz free energy density on  $\xi$  is the well-known double-well function used in many phase-field simulations,

$$f(\xi) = a \left( -\frac{1}{2}\xi^2 + \frac{1}{4}\xi^4 \right) \quad (3.12)$$

The overall driving force for the process, either  $\xi = 0 \rightarrow \xi = 1$ , or  $\xi = 0 \rightarrow \xi = -1$ , is

$$A = f(\xi = 0) - f(\xi = \pm 1) = \frac{a}{4} \quad (3.13)$$

The driving force at any intermediate state  $\xi$  between 0 and 1 is given by

$$A = -\frac{\partial f}{\partial \xi} = -a(-\xi + \xi^3) \quad (3.14)$$

We can then write down the kinetic evolution equation for  $\xi$  as

$$\frac{d\xi}{dt} = -L_\xi \frac{\partial f}{\partial \xi} = -L_\xi a(-\xi + \xi^3) = L_\xi a \xi (1 + \xi)(1 - \xi) \quad (3.15)$$

which is a nonlinear equation with respect to  $\xi$ . In general, such a nonlinear equation needs to be solved numerically. However, for the specific functional form of  $f$  in Eq. (3.12), we could solve Eq. (3.15) analytically. Rearranging Eq. (3.15), we have

$$\frac{1}{\xi(1 + \xi)(1 - \xi)} d\xi = L_\xi a dt \quad (3.16)$$

Integrating both sides of Eq. (3.16) from  $t = 0$  with a very small value of  $\xi_0$ , we get

$$\int_{\xi_0}^{\xi} \frac{1}{2} \left( \frac{2}{\xi} - \frac{1}{1 + \xi} + \frac{1}{1 - \xi} \right) d\xi = \int_0^t L_\xi a dt \quad (3.17)$$

or

$$\ln \frac{\xi^2}{\xi_0^2 (1 + \xi)(1 - \xi)} = 2L_\xi a t \quad (3.18)$$

For  $\xi \ll 1$ ,

$$\frac{\xi^2}{\xi_o(1+\xi)(1-\xi)} \approx \frac{\xi^2}{\xi_o^2} = e^{2L_\xi at} \quad (3.19)$$

or

$$\xi = \xi_o e^{L_\xi at} \quad (3.20)$$

which is the same result as Eq. (3.10) as expected. When  $t$  goes to infinite,

$$\frac{\xi_o(1+\xi)(1-\xi)}{\xi^2} = e^{-2L_\xi at} \rightarrow 0 \quad (3.21)$$

according to which the final state is either  $\xi \rightarrow -1$  or  $\xi \rightarrow +1$  as the equilibrium solution at the completion of the process.

As a final example of this section, let us consider the following tilted double-well energy function,

$$f(\xi) = a\xi^2(\xi-1)^2 - H(\xi)(f^\alpha - f^\beta) \quad (3.22)$$

where  $H(\xi)$  is called the interpolation function which has the following properties,

$$H(\xi) = \begin{cases} 0 & \text{for } \xi = 0 \\ 1 & \text{for } \xi = 1 \end{cases} \quad \text{and} \quad H'(\xi) = \begin{cases} 0 & \text{for } \xi = 0 \\ 0 & \text{for } \xi = 1 \end{cases} \quad (3.23)$$

The overall driving force for the process  $\xi = 0 \rightarrow \xi = 1$  is given by

$$A = f(\xi = 0) - f(\xi = 1) = f^\alpha - f^\beta \quad (3.24)$$

The driving force for an intermediate state  $\xi$  is given by

$$A(\xi) = -\frac{df}{d\xi} = -2a\xi(\xi-1)(2\xi-1) + H'(\xi)(f^\alpha - f^\beta) \quad (3.25)$$

We can write down a similar evolution equation based on linear kinetics,

$$\frac{d\xi}{dt} = -L_\xi \frac{df}{d\xi} = L_\xi [-2a\xi(\xi-1)(2\xi-1) + H(\xi)(f^\alpha - f^\beta)] \quad (3.26)$$

which can only be solved numerically.

#### 4. Isothermal heat and mass transport

The discussion in the last section is concerned with processes in a homogeneous system. However, in an inhomogeneous system, different types of matter including entropy, volume, and chemical substance can transport from one location to another. To avoid complexity, we will not discuss volume flow, which is important for applying the phase-field method to fluid systems. We will only discuss the diffusional transport equations of entropy and chemical substances, which are often coupled with phase-field equations in modeling the evolution of materials microstructures.

##### 4.1. Entropy or heat transport in a chemically uniform system

To connect the entropy or heat transport equation with the first and second laws of thermodynamics, let us consider a chemically homogeneous system in which the temperature is not uniform. The entropy or thermal energy will redistribute spatially driven by the temperature inhomogeneity. Let us assume that there are no other internal processes taking place at each local point other than the entropy redistribution or thermal energy transport. In this case, the rate of local thermal energy production in a volume element at temperature  $T$  under a temperature gradient  $\nabla T$  is given by

$$T \frac{ds^o}{dt} = -\nabla T \cdot \vec{J}_s \quad (4.1)$$

where  $ds^o/dt$  is the rate of entropy produced per unit volume, and  $\vec{J}_s$  is the entropy flux density.

Assuming linear kinetics, the entropy flux density  $\vec{J}_s$  is given by

$$\vec{J}_s = \frac{1}{T} \vec{J}_u = -\frac{k_Q}{T} \nabla T$$

where  $\vec{J}_u$  is the internal energy flux density at constant volume or the thermal energy flux density, and  $k_Q$  is the thermal conductivity. At constant volume, temperature can also be expressed as the derivative of internal energy with respect to entropy. Therefore, Eq. (4.2)

can also be rewritten as

$$\vec{J}_s = -\frac{k_Q}{T} \nabla T = -\frac{k_Q}{T} \nabla \frac{\partial u}{\partial s} \quad (4.3)$$

With the conservation equation for internal energy, we have

$$\frac{du}{dt} = -\nabla \cdot \vec{J}_u \quad (4.4)$$

Therefore, the evolution equation for entropy density is given by

$$T \frac{ds}{dt} = -\nabla \cdot \left( T \vec{J}_s \right) = \nabla \left[ k_Q \nabla \left( \frac{\partial u}{\partial s} \right) \right] \quad (4.5)$$

Using the relation  $ds = du/T = (c_v/T)dT$ , the above equation becomes the familiar heat conduction equation,

$$\frac{dT}{dt} = \frac{1}{c_v} \nabla \cdot (k_Q \nabla T) \quad (4.6)$$

where  $c_v$  is the constant volume heat capacity per unit volume, which can be written as the product of specific heat capacity, i.e., heat capacity per kg of mass and the mass density in terms of kg per unit volume.

#### 4.2. Isothermal diffusion kinetics

For an isothermal inhomogeneous system, if the only internal process is the redistribution of chemical species  $i$  at a constant uniform temperature,

$$df = \mu_i dc_i \quad (4.7)$$

where  $f$  is the Helmholtz free energy density. The rate of Helmholtz free energy density evolution is given by

$$\frac{df}{dt} = \mu_i \frac{dc_i}{dt} \quad (4.8)$$

For the redistribution of spatially inhomogeneous chemical species  $i$ , mass conservation requires that

$$\frac{dc_i}{dt} = -\nabla \cdot \vec{J}_i \quad (4.9)$$

Therefore,

$$\frac{df}{dt} = -\mu_i \nabla \cdot \vec{J}_i = -\nabla \cdot (\mu_i \vec{J}_i) + \nabla \mu_i \cdot \vec{J}_i \quad (4.10)$$

where the first term  $-\nabla \cdot (\mu_i \vec{J}_i)$  on the right-hand side is the exchange of chemical energy between the volume element and its neighboring elements whereas the second term  $\nabla \mu_i \cdot \vec{J}_i$  is the chemical energy dissipation due to the chemical transport flux density  $\vec{J}_i$  driven by the chemical potential gradient  $\nabla \mu_i$ . If we assume linear kinetics, we have

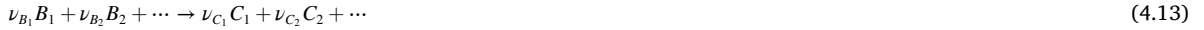
$$\vec{J}_i = -M_{ij} \nabla \mu_j \quad (4.11)$$

where  $M_{ij}$  is the mobility matrix describing the magnitude of the flux density of species  $i$  due to the chemical potential gradient of species  $j$ . Therefore, if there is inhomogeneity in chemical potentials, the system will evolve to reduce its total free energy  $F$  through the following diffusion equation,

$$\frac{dc_i}{dt} = \nabla \cdot (M_{ij} \nabla \mu_j) = \nabla \cdot \left( M_{ij} \nabla \frac{\partial f}{\partial c_j} \right) \quad (4.12)$$

#### 4.3. Isothermal chemical redistribution with reaction

Often chemical redistribution and chemical reactions take place simultaneously. For a general chemical reaction,



The driving force for the reaction is

$$A = \sum_i \nu_{B_i} \mu_{B_i} - \sum_j \nu_{C_j} \mu_{C_j} \quad (4.14)$$

where  $\mu_{B_i}$  and  $\mu_{C_j}$  are the chemical potentials of reacting species  $B_i$  and product species  $C_j$ , respectively. The magnitude of the internal process parameter describes the degree of reaction  $\xi$ .

If diffusion and reaction take place simultaneously, the mass conservation requires that

$$\frac{df}{dt} = \mu_i \frac{dc_i}{dt} = \mu_i \left( -\nabla \cdot \vec{J}_i + \frac{dc_i^o}{dt} \right) = -\mu_i \nabla \cdot \vec{J}_i - A \frac{d\xi}{dt} \quad (4.15)$$

We can rewrite the above equation as

$$\frac{df}{dt} = -\nabla \cdot \left( \mu_i \vec{J}_i \right) + \nabla \mu_j \cdot \vec{J}_i - A \frac{d\xi}{dt} \quad (4.16)$$

The first term at the right-hand side of the above equation is the chemical energy exchange between the volume element and its surrounding elements whereas the second term is the chemical energy dissipation rate due to chemical diffusion driven by the chemical potential gradient within the volume element, and the last term is the chemical energy dissipation due to the chemical reaction within the volume element. If we assume linear kinetics for both the chemical reaction and diffusion kinetics, we have

$$\frac{d\xi}{dt} = L_\xi A = -L_\xi \frac{\partial f}{\partial \xi} \quad (4.17)$$

and

$$\vec{J}_i = -M_{ij} \nabla \mu_j = -M_{ij} \nabla \frac{\partial f}{\partial c_j} \quad (4.18)$$

The local production or depletion rate of species  $i$  due to the chemical reaction is then given by

$$\frac{dc_i^o}{dt} = \nu_i \frac{dc_i}{dt} = -\nu_i L_\xi \frac{\partial f}{\partial \xi} \quad (4.19)$$

where  $\nu_i$  is  $-\nu_{B_i}$  for a reactant, and it is  $+\nu_{C_i}$  for a product. The concentration evolution with both diffusion and chemical reaction is then given by

$$\frac{dc_i}{dt} = -\nabla \cdot \vec{J}_i + \frac{dc_i^o}{dt} \quad (4.20)$$

or

$$\frac{dc_i}{dt} = \nabla \cdot \left( M_{ij} \nabla \frac{\partial f}{\partial c_j} \right) - \nu_i L_\xi \frac{\partial f}{\partial \xi} \quad (4.21)$$

## 5. Allen-Cahn equation

The Allen-Cahn equation is the primary equation for describing both phase transitions, driven by bulk free energy reduction, and the coarsening of domains formed during phase transitions, driven by interfacial energy reduction. It governs the evolution of a non-conserved phase field  $\xi$  characterizing the differences between phases, domains or grains of different crystallographic orientations. To connect the Allen-Cahn equation with the first and second laws of thermodynamics, let us consider the differential form for the Helmholtz free energy density,

$$df = -sdT + \mu_i dc_i + \gamma dA_v - Ad\xi \quad (5.1)$$

where  $A$  is the driving force for a phase transition. At uniform temperature and chemical composition for a closed system, Eq. (5.1) is reduced to

$$df = \gamma dA_v - Ad\xi \quad (5.2)$$

The change in interfacial area density  $A_v$  within the system is also an internal process. In the diffuse-interface description of the phase-field method, we include the thermodynamics of both processes, phase transition driven by a bulk free energy reduction and domain pattern coarsening driven by interfacial energy reduction, in a single total free energy functional by considering the dependence of the local free energy not only on the local order parameter  $\xi$  but also on its immediate environment described by the gradient  $\nabla \xi$ , i.e.,

$$F = \int [f(\xi) + f_{grad}(\nabla \xi)] dV \quad (5.3)$$

We typically consider only up to the second order in gradient  $\nabla \xi$  for the gradient energy, and hence

$$F = \int \left[ f(\xi) + \frac{1}{2} \kappa_\xi (\nabla \xi)^2 \right] dV \quad (5.4)$$

where  $f(\xi)$  is the homogeneous free energy density, and the second term is gradient energy with  $\kappa_\xi$  the gradient energy coefficient.

The overall driving force  $A$  including the interfacial energy contribution is then given by

$$A = -\frac{\delta F}{\delta \xi} = -\left( \frac{\partial f}{\partial \xi} - \kappa_\xi \nabla^2 \xi \right) \quad (5.5)$$

Therefore, assuming linear kinetics, the evolution of  $\xi$  is given by

$$\frac{d\xi}{dt} = L_\xi A = -L_\xi \frac{\delta F}{\delta \xi} = -L_\xi \left( \frac{\partial f}{\partial \xi} - \kappa_\xi \nabla^2 \xi \right) \quad (5.6)$$

which is essentially the Allen-Cahn equation [96].

The interfacial energy per unit area can be obtained by considering a one-dimensional system with a unit cross-sectional area:

$$\gamma = \int_{-\infty}^{+\infty} \left[ f(\xi) - f(\xi^{eq}) + \frac{\kappa_\xi}{2} \left( \frac{d\xi}{dx} \right)^2 \right] dx = \int_{-\infty}^{+\infty} \left[ \Delta f(\xi) + \frac{\kappa_\xi}{2} \left( \frac{d\xi}{dx} \right)^2 \right] dx \quad (5.7)$$

where  $f(\xi^{eq})$  is the local free energy density at equilibrium with order parameter  $\xi^{eq}$ .

At equilibrium

$$\frac{\partial \Delta f(\xi)}{\partial \xi} - \kappa_\xi \nabla^2 \xi = 0 \quad (5.8)$$

which can be rewritten as

$$\Delta f(\xi) = \frac{\kappa_\xi}{2} \left( \frac{d\xi}{dx} \right)^2 \quad (5.9)$$

Therefore, the interfacial energy can be rewritten as

$$\gamma = 2 \int_{-\infty}^{+\infty} \Delta f(\xi) dx = \int_{-\infty}^{+\infty} \kappa_\xi \left( \frac{d\xi}{dx} \right)^2 dx = \int_{-\xi^{eq}}^{+\xi^{eq}} \left[ \sqrt{2\kappa_\xi \Delta f(\xi)} \right] d\xi \quad (5.10)$$

One can also estimate the interfacial width  $l$  by noting that

$$\frac{d\xi}{dx} = \sqrt{\frac{2\Delta f}{\kappa_\xi}} \quad (5.11)$$

At the interfacial position  $\xi = 0$  between domain  $-\xi^{eq}$  and  $+\xi^{eq}$

$$\left( \frac{d\xi}{dx} \right)_{\xi=0} = \sqrt{\frac{2\Delta f}{\kappa_\xi}} \approx \frac{2\xi^{eq}}{l} \quad (5.12)$$

Solving Eq. (5.12) for  $l$ , we have

$$l = \sqrt{\frac{2\kappa_\xi \xi^{eq}}{\Delta f}} \quad (5.13)$$

As an example of applying the Allen-Cahn equation to the motion of an interface, let us consider the one-dimensional motion of a flat interface driven by a small external field. The Helmholtz free energy density is described by a tilted double-well potential

$$f(\xi) = (\xi + 1)^2 (\xi - 1)^2 + H(\xi)h \quad (5.14)$$

where  $h$  is a small positive constant, and

$$H(\xi) = \begin{cases} -1 & \text{for } \xi = -1 \\ +1 & \text{for } \xi = +1 \end{cases} \quad \text{and} \quad H'(\xi) = \begin{cases} 0 & \text{for } \xi = -1 \\ 0 & \text{for } \xi = +1 \end{cases} \quad (5.15)$$

The evolution equation for the order parameter is then given by

$$\frac{d\xi}{dt} = -4\xi(\xi + 1)(\xi - 1) + \kappa_\xi \nabla^2 \xi + H'(\xi)h \quad (5.16)$$

Let us consider the motion of an interface along  $x$ -direction between a domain described by  $\xi = -1$  and another domain described by  $\xi = +1$ . The velocity at constant  $\xi$  is given by

$$v = \left( \frac{dx}{dt} \right)_\xi = - \left( \frac{d\xi}{dt} \right)_x / \left( \frac{d\xi}{dx} \right)_t \quad (5.17)$$

With the above equation, we can rewrite Eq. (5.16) as

$$\left( \frac{d\xi}{dt} \right)_x = -v \left( \frac{d\xi}{dx} \right)_t = -4\xi(\xi+1)(\xi-1) + H'(\xi)h + \kappa_\xi \nabla^2 \xi \quad (5.18)$$

Multiplying both sides of the above equation by  $-d\xi/dx$ , we have

$$v \left( \frac{d\xi}{dx} \right)^2 = [4\xi(\xi+1)(\xi-1) - H'(\xi)h - \kappa_\xi \nabla^2 \xi] \frac{d\xi}{dx} \quad (5.19)$$

Integrating the above equation from  $-\infty$  to  $+\infty$  and employing the following boundary condition

$$\frac{d\xi}{dx} = 0 \quad \text{for } x \rightarrow \pm\infty, \quad (5.20)$$

we obtain the solution

$$v \int_{-\infty}^{+\infty} \left( \frac{d\xi}{dx} \right)^2 dx = -2h \quad (5.21)$$

Therefore,

$$v = - \frac{2h}{\int_{-\infty}^{+\infty} \left( \frac{d\xi}{dx} \right)^2 dx} \quad (5.22)$$

Replacing the integration in the denominator by the interfacial energy for an equilibrium interface per unit area using the following expression

$$\gamma = \kappa_\xi \int_{-\infty}^{+\infty} \left( \frac{d\xi}{dx} \right)^2 dx, \quad (5.23)$$

the velocity can be rewritten as

$$v = - \frac{2h\kappa_\xi}{\gamma} \quad (5.24)$$

The position for the interface as a function of time is given by

$$x_{\xi=0} = - \frac{2h\kappa_\xi}{\gamma} t \quad (5.25)$$

This simple analytical model can be employed to examine the accuracy of different numerical solutions to the Allen-Cahn equation.

As a final illustrative example, let us consider a simple case of a circular domain embedded in another domain to demonstrate the description of curvature-driven interface motion by the Allen-Cahn equation. Using the polar coordinates in two dimensions with the radial dimension labeled by  $r$ , the Allen-Cahn equation can be written as

$$\frac{1}{L_\xi} \frac{d\xi}{dt} = \kappa_\xi \left( \frac{\partial^2 \xi}{\partial r^2} + \frac{1}{r} \frac{\partial \xi}{\partial r} \right) - \frac{\partial f}{\partial \xi} \quad (5.26)$$

If the velocity at constant  $\xi$  surface at the domain wall is  $v$ , we can rewrite the above equation as

$$\frac{1}{L_\xi} \frac{dx}{dt} \frac{d\xi}{dr} = \frac{v}{L_\xi} \frac{d\xi}{dr} = \kappa_\xi \left( \frac{\partial^2 \xi}{\partial r^2} + \frac{1}{r} \frac{\partial \xi}{\partial r} \right) - \frac{\partial f}{\partial \xi} \quad (5.27)$$

Assuming that the radius  $R$  of the circular domain is much greater than the domain-wall thickness  $l$  ( $R \gg l$ ), multiplying both sides of the Eq. (5.27) by  $d\xi/dr$ , and integrating it with respect to  $r$  from 0 to  $\infty$ , and employing the following boundary conditions:

$$\frac{d\xi}{dr} = 0, \xi = -1, \text{at } r = 0 \quad (5.28)$$

$$\frac{d\xi}{dr} = 0, \xi = +1, \text{at } r \rightarrow \infty, \quad (5.29)$$

we have

$$v = \frac{dR}{dt} = - \frac{L_\xi \kappa_\xi}{R} \quad (5.30)$$

where  $1/R$  is the curvature of the circular domain. By further integrating the above equation with respect to time, we get the expected parabolic dependence of the radius of the circular domain on time from curvature-driven interface migration,

$$R^2 = R_o^2 - 2L_\xi K_\xi t \quad (5.31)$$

This analytical solution can also be employed to test the accuracy of numerical solutions to the Allen-Cahn Equation.

## 6. Cahn-Hilliard equation

We consider an isothermal system with an inhomogeneous distribution of chemical species. The possible energy dissipating internal processes within such a system include compositional phase separation of a homogeneous solution into solutions with different chemical compositions or vice versa, compositional redistribution due to local chemical potential inhomogeneity, and changes in the interfacial area density between the phases with different compositions, all of which are irreversible processes within a given volume element.

At constant temperature, the change in the Helmholtz free energy density with changes in local chemical concentration and interfacial area density can be written as

$$df = \mu_i dc_i + \gamma dA_v \quad (6.1)$$

The time evolution of the local Helmholtz free energy density is then given by

$$\frac{\partial f}{\partial t} = \mu_i \frac{\partial c_i}{\partial t} + \gamma \frac{\partial A_v}{\partial t} \quad (6.2)$$

Assuming there are no chemical reactions taking place in the system, the local conservation of chemical matter requires that

$$\frac{\partial c_i}{\partial t} = -\nabla \cdot \vec{J}_i \quad (6.3)$$

where  $\vec{J}_i$  is the mass flux density of species  $i$ . Therefore, the rate of change for the local Helmholtz free energy density can also be written as

$$\frac{\partial f}{\partial t} = -\mu_i \nabla \cdot \vec{J}_i + \gamma \frac{\partial A_v}{\partial t} \quad (6.4)$$

The above equation can be rewritten as

$$\frac{\partial f}{\partial t} = -\nabla \cdot \left( \mu_i \vec{J}_i \right) + \left( \nabla \mu_i \cdot \vec{J}_i + \gamma \frac{\partial A_v}{\partial t} \right) \quad (6.5)$$

where the first term of the right-hand side represents the rate of exchange of chemical energy between the volume element and its surrounding elements, and the rest two terms are the rates of dissipative changes driven by chemical potential inhomogeneity and interfacial energy reduction.

The time dependence of the total Helmholtz free energy of the system is

$$\frac{\partial F}{\partial t} = \int \left[ -\nabla \cdot \left( \mu_i \vec{J}_i \right) + \left( \nabla \mu_i \cdot \vec{J}_i + \gamma \frac{\partial A_v}{\partial t} \right) \right] dV \quad (6.6)$$

For a closed system with no flux of chemical species across the surfaces of the system, integration of the first term in Eq. (6.6) is zero. Therefore, the rate of Helmholtz free energy dissipation for the entire closed system is

$$\frac{\partial F^\circ}{\partial t} = \int \left[ (\nabla \mu_i) \cdot \vec{J}_i + \gamma \frac{\partial A_v}{\partial t} \right] dV \quad (6.7)$$

The rate of chemical energy to thermal energy conversion is given by

$$T \frac{dS^\circ}{dt} = -\frac{dF^\circ}{dt} = -\int \left[ (\nabla \mu_i) \cdot \vec{J}_i + \gamma \frac{\partial A_v}{\partial t} \right] dV \quad (6.8)$$

In the diffuse-interface description, the amount of chemical energy dissipation through compositional and internal interfacial area evolution processes is written as a single total free energy functional by considering the dependence of the local free energy not only on the local concentration  $c_i$  but also on its gradient  $\nabla c_i$ , i.e.,

$$F = \int [f(c_i) + f_{grad}(\nabla c_i)] dV \quad (6.9)$$

where  $F$  is the total Helmholtz free energy of the system. To approximate the gradient energy contribution up to the second order in gradient, a simple form is

$$F = \int \left[ f(c_i) + \frac{1}{2} \kappa_{c_i} (\nabla c_i)^2 \right] dV \quad (6.10)$$

where  $\kappa_{c_i}$  is the gradient energy coefficient.

The chemical potential relative to the final equilibrium state, including the gradient energy contribution, becomes

$$\dot{\mu}_i = \frac{\delta F}{\delta c_i} = \frac{\partial f(c_i)}{\partial c_i} - \kappa_{c_i} \nabla^2 c_i \quad (6.11)$$

If we assume linear kinetics,

$$\vec{J}_i = -M_{ij} \nabla \dot{\mu}_j = -M_{ij} \frac{\delta F}{\delta c_j} = -M_{ij} \left[ \frac{\partial f(c_j)}{\partial c_j} - \kappa_{c_j} \nabla^2 c_j \right]$$

where  $M_i$  is the diffusional mobility of species  $i$ . The mass conservation requires that

$$\frac{dc_i}{dt} = -\nabla \cdot \vec{J}_i \quad (6.12)$$

Therefore, we have the Cahn-Hilliard equation [95],

$$\frac{dc_i}{dt} = -\nabla \cdot \vec{J}_i = \nabla \cdot M_{ij} \nabla \frac{\delta F}{\delta c_j} = \nabla \cdot M_{ij} \nabla \left( \frac{\partial f}{\partial c_j} - \kappa_{c_j} \nabla^2 c_j \right) \quad (6.13)$$

The energy dissipation and entropy production rates are given by

$$T \frac{dS^o}{dt} = -\frac{dF^o}{dt} = -\int \nabla \dot{\mu}_i \cdot \vec{J}_i dV = \int M_i (\nabla \dot{\mu}_i)^2 dV \quad (6.14)$$

The interfacial free energy of a flat interface with its normal along the  $x$ -axis is given by

$$\gamma = \int_{-\infty}^{+\infty} \left[ \Delta f + \frac{1}{2} \kappa_{c_i} (\nabla c_i)^2 \right] dx \quad (6.15)$$

where  $\Delta f = f(c_i) - f(c_i^{eq})$  with  $c_i^{eq}$  the concentration profile at equilibrium.

At equilibrium,

$$\Delta f = \frac{1}{2} \kappa_{c_i} (\nabla c_i)^2 \quad (6.16)$$

Therefore, the interfacial energy between a phase with equilibrium composition  $c_{i,\alpha}^{eq}$  and another with equilibrium composition  $c_{i,\beta}^{eq}$  can also be rewritten as

$$\gamma = 2 \int_{-\infty}^{+\infty} \Delta f(c_i) dx = \int_{-\infty}^{+\infty} \kappa_{c_i} (\nabla c_i)^2 dx = \int_{c_{i,\alpha}^{eq}}^{c_{i,\beta}^{eq}} \sqrt{2 \kappa_{c_i} \Delta f(c_i)} dc_i \quad (6.17)$$

## 7. Coupled Allen-Cahn and Cahn-Hilliard equations

Majority of the materials processes involve coupled internal processes taking place at a given location such as chemical reactions and structural phase transformations and processes taking place through exchanges of thermal, chemical, electrical and mechanical matter between different regions in a system. For example, phase transformations such as precipitation reactions in solid solutions often require both atomic ordering taking place at a given location and compositional phase separation through compositional redistribution among different spatial regions. The modeling of such processes within the phase-field method requires the solution of a set of coupled Allen-Cahn and Cahn-Hilliard equations.

The corresponding differential form of the Helmholtz free energy density  $f$  of a system involving both non-conserved and conserved processes at constant temperature is given by

$$df = \mu_i dc_i + \gamma dA_v - A d\xi \quad (7.1)$$

The rate of Helmholtz free energy change per unit volume is

$$\frac{\partial f}{\partial t} = \mu_i \frac{\partial c_i}{\partial t} + \gamma \frac{\partial A_v}{\partial t} - A \frac{\partial \xi}{\partial t} \quad (7.2)$$

Using the mass conservation condition, we can rewrite the above equation as

$$\frac{\partial f}{\partial t} = -\mu_i \nabla \cdot \vec{J}_i + \gamma \frac{\partial A_v}{\partial t} - A \frac{\partial \xi}{\partial t} \quad (7.3)$$

which can be rewritten as

$$\frac{\partial f}{\partial t} = -\nabla \cdot \left( \mu_i \vec{J}_i \right) + \nabla \mu_i \cdot \vec{J}_i + \gamma \frac{\partial A_v}{\partial t} - A \frac{\partial \xi}{\partial t} \quad (7.4)$$

The rate of total Helmholtz free energy dissipation for a closed system is given by

$$\frac{\partial F^o}{\partial t} = \int \left[ \nabla \mu_i \cdot \vec{J}_i + \gamma \frac{\partial A_v}{\partial t} - A \frac{\partial \xi}{\partial t} \right] dV \quad (7.5)$$

In principle, we can write down three separate kinetic evolution equations for the redistribution of chemical species driven by the chemical potential gradient, interfacial area density evolution driven by the interfacial energy reduction, and the evolution of the order parameter  $\xi$  driven by  $A$ . However, in the diffuse-interface description, the local free energy is expressed as a function of composition and order parameter and their gradients rather than explicitly model the interfacial area evolution, i.e.,

$$F = \int [f(c_i, \xi) + f_{grad}(\nabla c_i, \nabla \xi)] dV \quad (7.6)$$

To the second order in gradients, we have

$$F = \int \left[ f(c_i, \xi) + \frac{1}{2} \kappa_{c_i} (\nabla c_i)^2 + \frac{1}{2} \kappa_\xi (\nabla \xi)^2 \right] dV \quad (7.7)$$

While the change of order parameter describing the internal process takes place locally within the volume element  $dV$ , the evolution of the local concentration should satisfy the local conservation equation. Therefore, the coupled evolution of the order parameter and concentration are given by

$$\frac{d\xi}{dt} = -L_\xi \frac{\delta F}{\delta \xi} = -L_\xi \left( \frac{\partial f}{\partial \xi} - \kappa_\xi \nabla^2 \xi \right) \quad (7.8)$$

$$\frac{dc_i}{dt} = \nabla \cdot M_i \nabla \frac{\delta F}{\delta c_i} = \nabla \cdot M_i \nabla \left( \frac{\partial f}{\partial c_i} - \kappa_{c_i} \nabla^2 c_i \right) \quad (7.9)$$

where  $L_\xi$  is relaxation constant for the order parameter, and  $M_i$  is the chemical mobility.

The corresponding interfacial energy of a flat interface with its normal along the  $x$ -direction between two phases described by both compositional and order parameter fields is

$$\gamma = \int_{-\infty}^{+\infty} \left[ f[c_i, \xi] - f[c_i^{eq}, \xi^{eq}] + \frac{1}{2} \kappa_{c_i} (\nabla c_i)^2 + \frac{1}{2} \kappa_\xi (\nabla \xi)^2 \right] dx \quad (7.10)$$

where the one-dimensional integration is carried out along the normal to the interface.

## 8. Microscopic diffusion equations – Microscopic phase-field method

A microscopic version of the continuum phase-field method is based on microscopic diffusion equations by Khachaturyan [88,89]. It was first applied to modeling the spinodal phase separation in a one-dimensional model system [89], and then to the kinetics of ordering and phase separation and the accompanying morphological evolution in binary alloy systems [22,98,99], vacancy ordering in the high-temperature oxide superconductor [100], effect of strain energy on precipitate shape evolution and interactions [98,101], and more recently to medium entropy alloys [102]. In this approach, the state of a non-equilibrium state is described by a set of probability distribution functions which characterize the probability of finding a particular atomic configuration at a given time. The temporal evolution of probability distribution functions describes the kinetics of diffusional processes and microstructure evolution of a solid solution on the underlying crystalline lattice.

We denote the set of single-site, pair, triplet, etc., probability distribution functions using

$$P_\alpha(\vec{r}), P_{\alpha\beta}(\vec{r}_i, \vec{r}_j), \dots \quad (8.1)$$

where  $P_\alpha(\vec{r})$  is the single-site occupation probability of finding species  $\alpha$  at lattice site  $\vec{r}$ ,  $P_{\alpha\beta}(\vec{r}_i, \vec{r}_j)$  is the joint probability of finding species  $\alpha$  at  $\vec{r}_i$  and species  $\beta$  at  $\vec{r}_j$ , etc. The distribution functions satisfy the normalization conditions,

$$\sum_\alpha P_\alpha(\vec{r}) = 1, \sum_{\beta\neq\alpha} P_{\alpha\beta}(\vec{r}_i, \vec{r}_j) = P_\alpha(\vec{r}_i), \dots \quad (8.2)$$

For simplicity, we consider the simplest possible atomic mechanism for diffusion, the direct exchange mechanism by ignoring the presence of vacancies, although it is straightforward to consider the vacancy mechanism, and it is possible to include higher order approximations, e.g., the pair approximation [103]. The direct exchange mechanism is unrealistic for diffusion in a substitutional solid

solution, but the ideas and concepts on the thermodynamics and kinetics illustrated in the exchange mechanism are essentially the same for the vacancy mechanism since vacancies can simply be viewed as another species. For the exchange mechanism in a binary system with two types of species  $\alpha$  and  $\beta$ , one only needs to write down one microscopic diffusion equation since  $P_\alpha(\vec{r}) + P_\beta(\vec{r}) = 1.0$ .

Assuming linear kinetics, the rate of change for the single-site occupation probability is linearly proportional to the thermodynamic driving force

$$\frac{dP_\alpha(\vec{r})}{dt} = \sum_{\vec{r}'} L(\vec{r} - \vec{r}') \frac{\partial F}{\partial P_\alpha(\vec{r}')} \quad (8.3)$$

where  $L(\vec{r} - \vec{r}')$  is the Onsager-type of linear kinetic coefficient matrix,  $t$  is time, and  $F$  is the total Helmholtz free energy of a spatial distribution of  $P_\alpha(\vec{r})$ .

Since the total number of atoms is conserved, the sum of the single-site occupation probabilities for  $\alpha$  over all the lattices is equal to the total number of  $\alpha$  atoms in the system, i.e.,

$$\sum_{\vec{r}} P_\alpha(\vec{r}, t) = N_\alpha = x_\alpha^o N \quad (8.4)$$

where  $N_\alpha$  is the total number of  $\alpha$  atoms,  $x_\alpha^o$  is the overall mole fraction of  $\alpha$  atoms, and  $N$  is the total number of lattice sites. Summing both sides of Eq. (8.3) over all atom sites  $\vec{r}$  and using the fact that  $N_\alpha$  is a constant give the following identity,

$$\sum_{\vec{r}} L(\vec{r}) \sum_{\vec{r}'} \frac{\partial F}{\partial P_\alpha(\vec{r}')} = 0 \quad (8.5)$$

Since the second summation in Eq. (8.5) is nonzero for nonequilibrium systems, the conservation condition for the total number of atoms requires that the first term be zero, i.e.,

$$\sum_{\vec{r}} L(\vec{r}) = 0 \quad (8.6)$$

A simple example for  $F$  is the standard mean-field model,

$$F = \frac{1}{2} \sum_{\vec{r}} \sum_{\vec{r}'} w(\vec{r} - \vec{r}') P_\alpha(\vec{r}) P_\alpha(\vec{r}') + k_B T \sum_{\vec{r}} [P_\alpha(\vec{r}) \ln P_\alpha(\vec{r}) + (1 - P_\alpha(\vec{r})) \ln(1 - P_\alpha(\vec{r}))] \quad (8.7)$$

where  $w(\vec{r} - \vec{r}')$  are the pairwise effective interaction energies, and  $k_B$  is the Boltzmann constant.

If we express the occupation probability function using a Fourier series expansion, we can express the Helmholtz free energy as

$$F = \frac{1}{2} \sum_{\vec{k}} w(\vec{k}) |P_\alpha(\vec{k})|^2 + k_B T \sum_{\vec{r}} [P_\alpha(\vec{r}) \ln P_\alpha(\vec{r}) + (1 - P_\alpha(\vec{r})) \ln(1 - P_\alpha(\vec{r}))] \quad (8.8)$$

where

$$w(\vec{k}) = \frac{1}{N} \sum_{\vec{r}} w(\vec{r}) e^{-i \vec{k} \cdot \vec{r}} \quad (8.9)$$

$$P_\alpha(\vec{k}) = \frac{1}{N} \sum_{\vec{r}} P(\vec{r}) e^{-i \vec{k} \cdot \vec{r}} \quad (8.10)$$

We can also rewrite the microscopic diffusion equation in Fourier space

$$\frac{dP_\alpha(\vec{k}, t)}{dt} = L(\vec{k}) \left\{ \frac{\partial F}{\partial P_\alpha(\vec{r})} \right\}_{\vec{k}} \quad (8.11)$$

where

$$L(\vec{k}) = \frac{1}{N} \sum_{\vec{r}} L(\vec{r}) e^{-i \vec{k} \cdot \vec{r}}$$

A nonlinear version of the microscopic diffusion equation was proposed by Martin [104] in which, the atomic exchange rates are written as

$$\nu_{\alpha(\vec{r} \rightarrow \vec{r} + \delta)} = \nu_0 e^{-\frac{[\varphi_s - \varphi(\vec{r})]}{k_B T}}, \nu_{\alpha(\vec{r} + \delta \rightarrow \vec{r})} = \nu_0 e^{-\frac{[\varphi_s - \varphi(\vec{r} + \delta)]}{k_B T}} \quad (8.12)$$

where  $\vec{r} + \delta$  represents a nearest neighbor site of  $\vec{r}$ ,  $\varphi_s$  is the energy per atom of the atomic configuration when an exchanging atom is at the saddle point of the energy landscape between the initial site  $\vec{r}$  and the final site  $\vec{r} + \delta$ ,  $\varphi(\vec{r})$  represents the energy per atom of the

atomic configuration before the atom exchange, and  $\varphi(\vec{r} + \delta)$  represents the energy per atom of the atomic configuration after the atomic exchange (Fig. 1). Therefore, the evolution of the probability distribution function is

$$\frac{dP_\alpha(\vec{r})}{dt} = \sum_{\delta} P_\beta(\vec{r})P_\alpha(\vec{r} + \delta)\nu_o e^{-\frac{[\varphi_S - \varphi(\vec{r} + \delta)]}{k_B T}} - \sum_{\delta} P_\alpha(\vec{r})P_\beta(\vec{r} + \delta)\nu_o e^{-\frac{[\varphi_S - \varphi(\vec{r})]}{k_B T}} \quad (8.13)$$

A similar nonlinear microscopic diffusion equation was discussed by Le Boar and Khachaturyan [105]

$$\frac{dP_\alpha(\vec{r})}{dt} = \nu_o e^{-\frac{\varphi_S}{k_B T}} \left[ \sum_{\delta} P_\beta(\vec{r})P_\alpha(\vec{r} + \delta)e^{-\frac{[\varphi(\vec{r}) - \varphi(\vec{r} + \delta)]}{2k_B T}} - \sum_{\delta} P_\alpha(\vec{r})P_\beta(\vec{r} + \delta)e^{-\frac{[\varphi(\vec{r}) + \delta] - \varphi(\vec{r})}{2k_B T}} \right] \quad (8.14)$$

The set of interaction energies and associated atomic migration potential barriers in the microscopic model can be obtained by fitting the energetics of atomic configurations either to density function theory calculations or to experimentally measured thermodynamic properties. One of the main advantages of this approach is the fact that with the input of the effective interaction energies and activation barriers for atomic diffusion, the morphological evolution during diffusional ordering and phase separation can be automatically predicted without prior knowledge of possible transient and equilibrium phases by numerically solving the microscopic diffusion Eq. (8.3), or (8.13), or (8.14). Furthermore, the effects of long-range elastic [100,101,105,106] or electrostatic [107] interactions on the microstructure development can also be readily incorporated based on continuum elasticity and electrostatics.

## 9. From microscopic diffusion equations to continuum phase-field equations

The microscopic diffusion equations can be viewed as the microscopic versions of the continuum phase-field equations. As a matter of fact, one can obtain the continuum phase-field equations by performing continuum limits of the microscopic diffusion equations.

For compositional phase separation, the Fourier transform of the single-site occupation probability function has significant values only around the reciprocal lattice vector  $\vec{k} = 0$  with the real space length scale  $d$  of the composition domains related to the position of  $k_{max} (= 2\pi/d)$  for the maximum  $|P_\alpha(\vec{k})|^2$ . Therefore, we can perform a Taylor series expansion of  $L(\vec{k})$  around  $\vec{k} = 0$ ,

$$L(\vec{k}) = L(0) + \left[ \frac{\partial L(\vec{k})}{\partial k_i} \right]_{\vec{k}=0} k_i + \frac{1}{2!} \left[ \frac{\partial^2 L(\vec{k})}{\partial k_i \partial k_j} \right]_{\vec{k}=0} k_i k_j + \dots \quad (9.1)$$

where  $L(0)$  is the value of  $L(\vec{k})$  at  $\vec{k} = 0$ , which is zero from the conservation condition of atoms. The second term is also zero by symmetry. Therefore, the first non-vanishing term for the expansion of  $L(k)$  at  $\vec{k}$  close to 0 is the third term

$$L(\vec{k}) \approx \frac{1}{2!} \left[ \frac{\partial^2 L(\vec{k})}{\partial k_i \partial k_j} \right]_{\vec{k}=0} k_i k_j = -M_{ij} k_i k_j \quad (9.2)$$

We can also do a Taylor series expansion for  $w(\vec{k})$  around  $\vec{k} = 0$ ,

$$w(\vec{k}) \approx w(0) + \frac{1}{2!} \left[ \frac{\partial^2 w(\vec{k})}{\partial k_i \partial k_j} \right]_{\vec{k}=0} k_i k_j = w(0) - \frac{\kappa_{ij}^c}{2} k_i k_j \quad (9.3)$$

Similarly, if we perform a Taylor series expansion for  $w(\vec{k})$  around  $\vec{k} = \vec{k}_o$ , we have

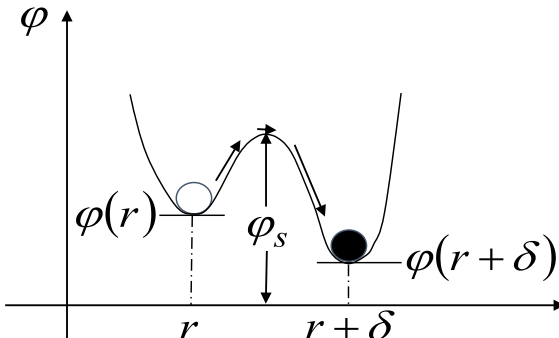


**Fig. 1.** Illustration of potential landscape for an atomic exchange.

$$w\left(\vec{k}_o + \vec{k}\right) \approx w\left(\vec{k}_o\right) + \frac{1}{2!} \left[ \frac{\partial^2 w\left(\vec{k}\right)}{\partial k_i \partial k_j} \right]_{\vec{k} = \vec{k}_o} k_i k_j = w\left(\vec{k}_o\right) - \frac{\kappa_{ij}^c}{2} k_i k_j \quad (9.4)$$

We can express Eq. (9.8) and (9.9) of Section 8 as a sum of a local free energy density as a function of  $c_a(\vec{r})$  and  $\eta(\vec{r})$  and the respective gradient energy associated with the gradients of  $c_a(\vec{r})$  and  $\eta(\vec{r})$ . The values of  $w(0)$  and  $w\left(\vec{k}_o\right)$  determine the tendency of an alloy towards phase separation and ordering with the superlattice vector  $\vec{k}_o$ , respectively, and  $\kappa_{ij}^c$  and  $\kappa_{ij}^\eta$  are the corresponding gradient energy coefficients given by

$$\kappa_{ij}^c = - \sum_r r_i r_j w(\vec{r}) \quad (9.5)$$

and

$$\kappa_{ij}^\eta = - \sum_r r_i r_j w(\vec{r}) e^{-i \vec{k}_o \cdot \vec{r}} \quad (9.6)$$

Eqs. (9.5) and (9.6) provide the relations to compute the gradient energy coefficients for composition  $\kappa_{ij}^c$  and long-range order parameter  $\kappa_{ij}^\eta$  in terms of effective interatomic interaction parameters  $w(\vec{r})$ .

Substituting Eq. (9.2) into Eq. (9.11) of Section 8, we have

$$\frac{dP_a(\vec{k}, t)}{dt} = - M_{ij} k_i k_j \left\{ \frac{\partial F}{\partial P_a(\vec{r})} \right\}_{\vec{k}} \quad (9.7)$$

The back-Fourier transform of Eq. (9.7) is

$$\frac{dP_a(\vec{r}, t)}{dt} = M_{ij} \nabla_i \nabla_j \frac{\delta F}{\delta P_a(\vec{r})} \quad (9.8)$$

For a compositional phase separation process,

$$P_a(\vec{r}, t) = x_a(\vec{r}, t) \quad (9.9)$$

where  $x_a$  is the mole fraction of  $\alpha$  atoms. Therefore, Eq. (9.8) can be rewritten as

$$\frac{dx_a(\vec{r}, t)}{dt} = M_{ij} \nabla_i \nabla_j \frac{\delta F}{\delta x_a(\vec{r})} \quad (9.10)$$

which is the Cahn-Hilliard equation with a constant diffusional mobility.

For the case of order-disorder process,  $|P_a(\vec{k})|^2$  has significant values only near  $\vec{k} = \vec{k}_o$  where  $\vec{k}_o$  is the superlattice vector of the corresponding ordered phase. Expressing the single-site occupation probability in terms of composition  $x_a$  and order parameter  $\eta(\vec{r})$ , we have

$$P_a(\vec{r}) = x_a + x_a \eta(\vec{r}) e^{i \vec{k}_o \cdot \vec{r}} \quad (9.11)$$

It can be shown that

$$P_a\left(\vec{k}_o + \vec{k}\right) = x_a \eta\left(\vec{k}\right) \quad (9.12)$$

The  $L\left(\vec{k}_o + \vec{k}\right)$  around  $\vec{k}_o$  can be approximated by

$$L\left(\vec{k}_o + \vec{k}\right) \approx L\left(\vec{k}_o\right) \quad (9.13)$$

Therefore, we can express the evolution of amplitudes of spatial variation in real space  $P_a(\vec{r}, t)$  in terms of the spatial variation of the long-range order parameter  $\eta(\vec{r}, t)$ ,

$$\frac{d\eta(\vec{r}, t)}{dt} = L\left(\vec{k}_o\right) \frac{\delta F}{\delta \eta(\vec{r}, t)} \quad (9.14)$$

which is essentially the Allen-Cahn equation with the gradient energy coefficient given by Eq. (9.6) in terms of effective interaction energies.

Therefore, the continuum Allen-Cahn and Cahn-Hilliard equations can be obtained from a continuum limit of the microscopic

diffusion equations. One of the advantages of the microscopic equations is the fact that it does not require any a priori assumption on the types of chemical ordering and decomposition that would occur, including the appearance of transient and metastable phases which might appear, along the evolution path of a nonequilibrium system once the values of the effective interchange energies and atomic migration barriers are determined, e.g., from the experiments or DFT calculations. One does not need to know in advance what the final equilibrium phases are. However, the continuum equations can be applied to a wide variety of materials processes, not limited to diffusion-controlled processes, whereas microscopic diffusion equations can only be applied to predicting diffusional transformations, such as atomic ordering and compositional clustering on a given crystalline lattice.

## 10. Phase-field crystal – Phase-field method at atomic scale

Phase-field crystal is another density-based approach at the atomic scale pioneered by Elder et al [86]. At the continuum limit, the thermodynamic description and kinetic evolution equations in the phase-field crystal are reduced to those in the conventional phase-field model with long-wave amplitudes as the order parameters or phase-fields [108,109]. They can also be considered as a set of microscopic diffusion equations generalized to the continuum space, i.e., while the microscopic diffusion equations are defined on the fixed lattice points of a crystalline solid, the atomic structure of a system in the phase-field crystal is described by an atomic density function  $\rho(\vec{r})$  in the continuum space [110]. A uniform atomic density distribution  $\rho_0$  in the phase-field crystal describes a liquid state while a periodic atomic density distribution represents a crystalline state with its maxima indicating the locations of atoms. The Fourier amplitudes of the periodical density distribution represent the structural amplitudes of a crystal, which have significant values only at and around the reciprocal lattice points of the crystal.

The thermodynamics of a system in the atomic density functional theory is described by the total Helmholtz free energy  $F$  as a functional of the atomic density function  $\rho(\vec{r})$ . An example of a simple free energy functional based on a pairwise interaction model [110] is

$$F = \int f[\rho(\vec{r})] d^3\vec{r} + \frac{1}{2} \iint w(\vec{r} - \vec{r}') \rho(\vec{r}) \rho(\vec{r}') d^3\vec{r} d^3\vec{r}', \quad (10.1)$$

where  $f[\rho(\vec{r})]$  is the local free energy density, and  $w(\vec{r} - \vec{r}')$  is the effective pairwise interaction energy or the direct two-particle correlation function [111]. The interaction term in Eq. (10.1) can be expressed in the Fourier space as in the microscopic diffusion model [110],

$$F = \int f[\rho(\vec{r})] d^3\vec{r} + \frac{1}{2} \int w(\vec{k}) |\rho(\vec{k})|^2 \frac{d^3\vec{k}}{(2\pi)^3} \quad (10.2)$$

where

$$w(\vec{k}) = \frac{1}{V} \int w(\vec{r}) \exp(-i\vec{k} \cdot \vec{r}) d^3\vec{r} \quad (10.3)$$

and

$$\rho(\vec{k}) = \frac{1}{V} \int \rho(\vec{r}) \exp(-i\vec{k} \cdot \vec{r}) d^3\vec{r} \quad (10.4)$$

Performing a Taylor series expansion of  $w(\vec{k})$  with respect to the average density at  $\vec{k} = 0$ , we have

$$w(\vec{k}) = A_o + A_2 k_i k_j + A_4 k_i k_j k_k k_l + \dots \quad (10.5)$$

where

$$A_o = w(0), A_2 = \frac{1}{2!} \left[ \frac{\partial^2 w(\vec{k})}{\partial k_i \partial k_j} \right]_{k=0}, A_4 = \frac{1}{4!} \left[ \frac{\partial^4 w(\vec{k})}{\partial k_i \partial k_j \partial k_k \partial k_l} \right]_{k=0}, \dots \quad (10.6)$$

Substituting Eqs. (10.5) and (10.6) back to Eq. (10.2), we have

$$F = \frac{1}{2} \int [A_o + A_2 k_i k_j + A_4 k_i k_j k_k k_l + \dots] |\rho(k)|^2 \frac{d^3\vec{k}}{(2\pi)^3} + \int f[\rho(\vec{r})] d^3\vec{r} \quad (10.7)$$

If we rewrite the interaction term in the above equation in the real space, we have

$$F = \int \left\{ \frac{1}{2} [A_o \rho^2(\vec{r}) - A_2 \nabla_i \rho(\vec{r}) \nabla_j \rho(\vec{r}) + A_4 \nabla_i \nabla_j \rho(\vec{r}) \nabla_k \nabla_l \rho(\vec{r}) + \dots] + f[\rho(\vec{r})] \right\} d^3\vec{r} \quad (10.8)$$

Truncating at the fourth-order term in  $k$  in Eq. (10.7) or the fourth order gradient in Eq. (10.8), recovers the original phase-field crystal model [86] or referred to as one mode phase-field crystal model while retaining all terms up to the eighth order in either Eq.

(10.7) or (10.8) leads to the two mode phase-field crystal model [112].

It is easy to see from Eq. (10.7) that the atomic density amplitudes  $|\rho(\vec{k})|^2$  are expected to grow in regions of the  $k$ -space where  $w(\vec{k})$  is negative. It is the instability of the uniform atomic density with respect to the amplitude of atomic density modulation that leads to the formation of stable atomic density patterns [108,111–113]. Therefore, the functional form of  $w(\vec{k})$  in Fourier space largely determines the periodic atomic structures in the real space. With an appropriate choice of  $A_0, A_2, A_4, \dots$ , a period distribution of  $\rho(\vec{r})$  represents a crystalline equilibrium state which minimizes the total free energy of the system.

The temporal evolution of the atomic density function can be written as an analog to the microscopic diffusion equation [110]

$$\frac{d\rho(\vec{r})}{dt} = \int L(\vec{r} - \vec{r}') \frac{\delta F[\rho(\vec{r}')] }{\delta \rho(\vec{r}')} d^3\vec{r}', \quad (10.9)$$

where  $F[\rho(\vec{r}')]$  is the Helmholtz free energy functional of  $\rho(\vec{r}')$ , and  $L(\vec{r} - \vec{r}')$  is related to the diffusional mobility of atoms from point  $\vec{r}$  to  $\vec{r}'$ . The only difference between Eqs. (10.3) of Section 8 and (10.9) here is the fact the probability distribution functions in the microscopic diffusion equations are only defined at discrete lattice points while the atomic density function in the phase-field crystal is defined for the continuum space.

Fourier transforming both sides of Eq. (10.9), we obtain the evolution equation for the amplitude of the atomic density function in the Fourier space,

$$\frac{d\rho(\vec{k})}{dt} = L(\vec{k}) \left\{ \frac{\delta F[\rho(\vec{r}')] }{\delta \rho(\vec{r}')} \right\}_{\vec{k}} \quad (10.10)$$

The mass conservation requires that

$$\int \rho(\vec{r}) d^3\vec{r} = N = \text{constant},$$

and thus

$$L(k) \approx L(\vec{k} = 0) + \frac{1}{2!} \left[ \frac{\partial^2 L(\vec{k})}{\partial k_i \partial k_j} \right]_{k=0} k_i k_j = -M_{ij} k_i k_j \quad (10.11)$$

The numerical solution to Eq. (10.10) yields the temporal spatial distribution of the density function,  $\rho(\vec{r})$ , and thus the atomic density configuration. Similar to the continuum limits of the microscopic diffusions leading to the Allen-Cahn and Cahn-Hilliard equations, one can also translate Eq. (10.10) into equations in terms of the amplitudes of atomic density modulations.

One of the main advantages for the phase-field crystal is the fact it combines the atomistic length scale with a diffusive time scale. It automatically takes into account of the possible generation of structural defects such as dislocations and grain boundaries without any a priori assumptions and the role of elasticity in the morphological evolution of defect and phase morphologies. It has been applied to modeling the morphological phenomena for a wide variety of processes as described in several review articles [87,114,115].

## 11. Contribution of stress, electric, and magnetic fields to microstructure evolution

The local structures and properties of an inhomogeneous solid are, by definition, spatially dependent at different scales. In the continuum treatment of a mesoscale microstructure, a volume element  $dV$  within a solid can be considered as a thermodynamic system. There can be internal local processes taking place within the volume element which generates local mechanical strain, polarization, or magnetization due to structural, ferroelectric or ferromagnetic phase transitions. At the meantime, the properties within each volume element not only depends on the local thermodynamic property densities but also are strongly influenced by the presence of mechanical, electric, and magnetic fields generated by surrounding volume elements within the solid due to the spatial distributions of lattice parameters, electric charges, polarization, and magnetization. As a matter of fact, it is the competition of local energy contributions such as interfacial energy and these long-range elastic, electric, and magnetic energy contributions to the thermodynamics are responsible for the formation and stability of many of the fascinating microstructure patterns. Therefore, to predict the microstructure evolution in a solid, it is important to incorporate the contributions of elastic, electric, and magnetic interactions to the thermodynamics of materials processes. It should be emphasized that we only consider the quasi-static elastic, electric, and magnetic fields which are obtained from the solutions to the elasticity, electrostatic and magnetostatic equilibrium equations for a given microstructure specified by phase-fields and order parameters.

For simplicity, let us consider a chemically uniform and closed thermodynamic system under isothermal, uniform temperature conditions. The differential form for the molar Helmholtz free energy  $f$  can be written as

$$df = \sigma_{ij} d\varepsilon_{ij} + E_i dD_i + H_i dB_i \quad (11.1)$$

If there are internal processes taking place involving the generation of spontaneous strain, or polarization, or magnetization, the

differential form can be rewritten as

$$df = \sigma_{ij}d\epsilon_{ij}^e + E_i dD_i^e + H_i dB_i^e + \left( \frac{\partial f}{\partial \epsilon_{ij}^o} \right) d\epsilon_{ij}^o + \left( \frac{\partial f}{\partial P_i^o} \right) dP_i^o + \left( \frac{\partial f}{\partial M_i^o} \right) dM_i^o \quad (11.2)$$

where  $d\epsilon_{ij}^e$ ,  $dD_i^e$ , and  $dB_i^e$  are changes in strain, electric polarization, and magnetization due to the presence of quasi-static local stress field  $\sigma_{ij}$ , electric field  $E_i$ , and magnetic  $H_i$ , whereas  $d\epsilon_{ij}^o$ ,  $dP_i^o$ , and  $dM_i^o$  are the spontaneous changes in strain, electric polarization, and magnetization as a result of structural, ferroelectric, and ferromagnetic phase transitions. Replacing  $\epsilon_{ij}^e$ ,  $D_i^e$ , and  $B_i^e$  in Eq. (11.2) with  $\epsilon_{ij} - \epsilon_{ij}^o$ ,  $D_i - P_i^o$ , and  $B_i - M_i^o$ , we have

$$df = \sigma_{ij}d(\epsilon_{ij} - \epsilon_{ij}^o) + E_i d(D_i - P_i^o) + H_i d(B_i - M_i^o) + \left( \frac{\partial f}{\partial \epsilon_{ij}^o} \right) d\epsilon_{ij}^o + \left( \frac{\partial f}{\partial P_i^o} \right) dP_i^o + \left( \frac{\partial f}{\partial M_i^o} \right) dM_i^o \quad (11.3)$$

in which both the total and spontaneous order parameters should be treated as independent thermodynamic variables.

If we assume linear relations between the quasi-static fields and corresponding instantaneous responses, we have

$$\sigma_{ij}(r) = C_{ijkl}[\epsilon_{kl}(r) - \epsilon_{kl}^o(r)] \quad (11.4)$$

$$D_i - P_i^o = \epsilon_o \kappa_{ij} E_j \quad (11.5)$$

$$B_i - M_i^o = \mu_o H_i \quad (11.6)$$

where  $C_{ijkl}$  is the fourth-rank elastic modulus tensor excluding any ferroelastic soft mode contribution,  $\kappa_{ij}$  is the background dielectric constant by excluding the contributions from the ferroelectric optical soft mode [116–119],  $\epsilon_o$  is the vacuum dielectric permittivity, and  $\mu_o$  is the vacuum magnetic permeability.

The Helmholtz free energy density can then be written as

$$f = \frac{1}{2}C_{ijkl}(\epsilon_{ij} - \epsilon_{ij}^o)(\epsilon_{kl} - \epsilon_{kl}^o) + \frac{1}{2}(\epsilon_o \kappa_{ij})^{-1}(D_i - P_i^o)(D_j - P_j^o) + \frac{1}{2\mu_o}(B_i - M_i^o)(B_j - M_j^o) + f^o(T, c_i, \epsilon_{ij}^o, P_i^o, M_i^o) \quad (11.7)$$

where  $\epsilon_{ij}$ ,  $D_i$ , and  $B_i$  are obtained by solving the mechanical, electrostatic, and magnetostatic equilibrium equations for a given set of spatial distributions of  $\epsilon_{ij}^o$ ,  $P_i^o$ , and  $M_i^o$ .

The mechanical equilibrium equation is given by

$$\frac{\partial \sigma_{ij}}{\partial r_j} = \frac{\partial}{\partial r_j} \{ C_{ijkl}[\epsilon_{kl}(\vec{r}) - \epsilon_{kl}^o(\vec{r})] \} = 0 \quad (11.8)$$

If we relate the heterogeneous strain to the displacements in the small strain approximation and assume a homogeneous  $C_{ijkl}$ , we can rewrite the mechanical equilibrium Eq. (11.8) as

$$C_{ijkl}\frac{\partial^2 u_k}{\partial r_j \partial r_l} = C_{ijkl}\frac{\partial \epsilon_{kl}^o(\vec{r})}{\partial r_j} \quad (11.9)$$

where  $u_k$  is heterogeneous mechanical displacements. In general,  $\epsilon_{kl}^o(\vec{r})$  can be produced from different types of sources such as compositional inhomogeneities, structural transformations, structural defects (specified by eigenstrain  $\epsilon^d(\vec{r})$ ), thermal mismatches, electromechanical strains, magnetostrictive strains, i.e.,

$$\epsilon_{ij}^o(\vec{r}) = \epsilon_{ij}^o[c_i(\vec{r}), \eta_i(\vec{r}), P_i^o(\vec{r}), M_i^o(\vec{r}), \epsilon^d(\vec{r}), \dots] \quad (11.10)$$

To obtain the electric displacement  $D_i$ , we first relate the quasistatic electric field  $E_i$  to the electric potential  $\phi$ ,  $E_i = -\nabla_i \phi$ , and obtain the electric potential by solving the electrostatic equilibrium equation, i.e., the Poisson equation,

$$-\nabla_i(\epsilon_o \kappa_{ij} \nabla_j \phi) = -\nabla_i P_i^o \quad (11.11)$$

where  $-\nabla_i P_i^o$  is the amount of bound charge due to the inhomogeneity of the spontaneous polarization in a ferroelectric domain structure. For a homogeneous dielectric constant, Eq. (11.11) becomes

$$-\epsilon_o \kappa_{ij} \nabla_i \nabla_j \phi = -\nabla_i P_i^o \quad (11.12)$$

The elastic and electrostatic equilibrium equations generally have to be solved numerically, e.g., using the spectral iterative method [120] or a finite element method. However, for the case of homogeneous elastic moduli and dielectric constant, both Eqs. (11.9) and (11.12) can be analytically solved in Fourier space for systems which can be approximated with periodic boundary conditions [89].

Using a similar line of analysis as for the electrostatic energy, we can introduce an artificial scalar magnetic potential  $\phi_{mag}$  analogous to the electric potential to write down the magnetostatic equilibrium equation as

$$-\mu_o \nabla^2 \phi_{mag} = -\nabla_i M_i^o \quad (11.13)$$

One of the main differences between ferromagnetics and ferroelectrics is the fact while the depolarization field in ferroelectrics can be compensated by free charges, there is no such compensation mechanism for the demagnetization energy in ferromagnetics. To consider the demagnetization energy, one approach is to separate the spatially dependent spontaneous magnetization into a sum of average magnetization and inhomogeneous magnetization. Analytical solutions exist for certain special geometries of a sample for determining the demagnetization energy based on the knowledge of average magnetization ( $\bar{M}_i^o$ ) while the inhomogeneous magnetization is obtained by solving the magnetostatic equilibrium equation,

$$-\mu_o \nabla^2 \phi_{mag} = -\nabla_i (\bar{M}_i^o + \delta M_i^o) = -\nabla_i (\delta M_i^o) \quad (11.14)$$

which can be solved analytically in the Fourier space [89]. The total local magnetic field is the sum of the magnetic field due to the local inhomogeneity of the magnetization distributions and the demagnetization field as well as the external field [121].

## 12. Simulation-guided discovery and optimization of microstructures and properties

One of the main advantages of the phase-field method is the fact that one can readily incorporate simultaneously chemical, thermal, electric, mechanical, and magnetic contributions to essentially all types of materials processes of interest. One can analyze the relative importance of their contributions to the formation, stability, and responses of microstructures to external stimuli by turning on and off one or more of them. Therefore, phase-field method has been applied to a diverse set of materials processes, including phase transformations, microstructure coarsening, mass and heat transport, and chemical reactions, as well as processes such as plastic deformation and domain switching. However, the majority of the existing applications of the phase-field method have been largely limited to idealized model systems for demonstrating the capability of a phase-field model or testing analytical theories with simplified assumptions. While there have been increasing efforts in employing phase-field simulations to help interpret and understand experimentally observed microstructures, there has been a lack of successful examples to use phase-field simulations help design and optimize materials microstructures and properties. Therefore, the brief discussions below will instead be entirely focused on a couple of very recent examples demonstrating the possibility of applying phase-field method to provide guidance to experimental synthesis to optimize properties or discover novel mesoscale microstructures or new functionalities.

As it will be seen below that close and iterative interactions between simulations and experiments are critical to realizing the true power of the phase-field method in the prediction and discovery of new materials phenomena and novel functionalities. Here we will discuss three examples of theory-guided discovery of new materials microstructures and functionalities or dramatic enhancement of properties: (I) the discovery of polar vortex lattices [122,123], skyrmions [124], and unusual negative capacitances [125] in ferroelectric superlattices, (II) synthesis of record-high piezoelectricity in ferroelectric relaxor ceramics [126,127], and (III) the discovery of simultaneous near-perfect light transparency and ultrahigh piezoelectricity in  $\text{Pb}(\text{Mg}_{1/3}\text{Nb}_{2/3})\text{O}_3\text{-PbTiO}_3$  (PMN-PT) crystals through alternative-current (AC) electric field poling [128]. The hope, through the discussions of these examples, is to stimulate shifting of our efforts in the phase-field community from demonstrating the capabilities of phase-field models and interpreting experimental results using phase-field modeling to providing guidance to experimental synthesis and characterization for discovering novel materials microstructures and properties by carefully designing phase-field simulation strategies.

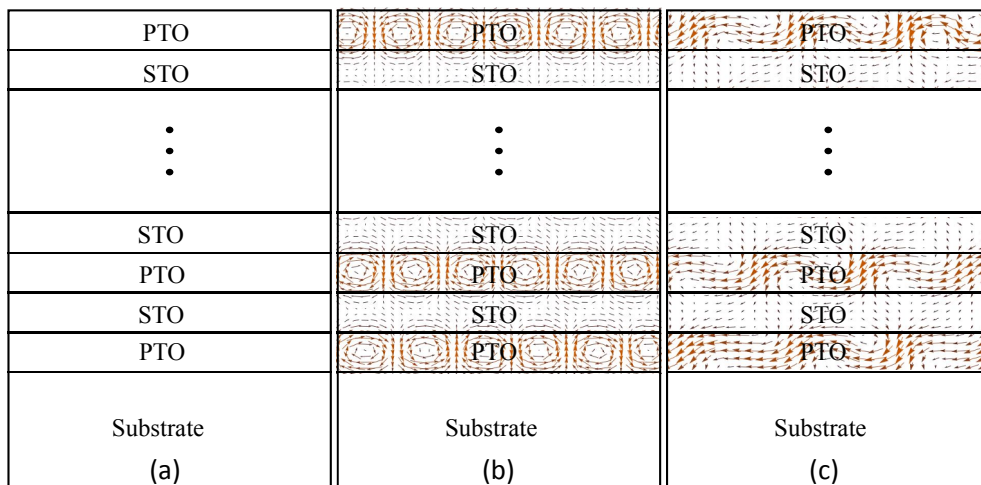


**Fig. 2.** (a) Schematic illustration of a superlattice thin film of (PTO)/STO on a substrate; (b) vortex arrays in the PTO layers in a  $(\text{PTO})_6/(\text{STO})_6$  superlattice; (c) wavy polarization distribution in the PTO layers  $(\text{PTO})_6/(\text{STO})_6$  superlattice with a 0.6 V built-in voltage. Extracted from previously unpublished results with permission from Zijian Hong.

### 12.1. Discovery of novel polar vortex lattice in ferroelectric superlattices

Here we first discuss an example of how phase-field modeling, in close collaboration with experimentalists, has been utilized to discover novel polar structures including polar vortex lattice, mixture of vortex lattice and ferroelastic twins, skyrmions, and topological transformations under external stimuli as well as novel properties such as negative dielectric capacitance [122–125]. The discovered topological polar states and the fundamental understanding of their phase transitions and properties could be potentially utilized for future electronic applications.

The particular example is a superlattice consisting of several unit cells of  $\text{PbTiO}_3$  (PTO) and several unit cells of  $\text{SrTiO}_3$  (STO), both of which are of the perovskite structure, periodically repeating along the [001] crystallographic direction (See Fig. 2(a)) for illustration of such a superlattice on a substrate). Experimental growth techniques are now sufficiently advanced that nearly atomic perfect oxide superlattices with coherent interfaces between the layers can be grown on different substrates with no noticeable structural defects such as misfit dislocations.

At room temperature,  $\text{PbTiO}_3$  is a classic ferroelectric with tetragonal symmetry and with spontaneous polarizations along the tetragonal axis while  $\text{SrTiO}_3$  is a paraelectric. One of the questions is what happens to the electric polarization distribution when the  $\text{PbTiO}_3$  layers are confined between  $\text{SrTiO}_3$  layers within the superlattice thin film on a substrate.

The computational effort started with an attempt to reproduce the experimental observation of wave-like polarization distributions in a  $(\text{PTO})_6/(\text{STO})_6$  superlattice with 6 unit-cells of PTO and 6 unit-cells of STO repeating along the [001] thickness direction. As it turned out, we obtained an array of vortices in the  $\text{PbTiO}_3$  layers instead (Fig. 2(b)) based on available materials parameters such as free energy density as a function of polarization, lattice parameters, elastic constants, and domain wall energy. After more than a month of effort without success to obtain the wavy polarization distribution, we decided to introduce a built-in voltage bias which commonly exists in oxide thin films due to the difference in the electronic properties of the surface of a superlattice film and the film/substrate interface. Indeed, an introduction of 0.6 V built-in voltage beautifully reproduces not only the experimentally observed wave-like polarization distribution (Fig. 2(c)) but also the observed complicated mixture of twins consisting of domains with in-plane polarization directions and the wavy polarization distributions. One of the advantages of the phase-field simulations is the fact that one can readily perform systematic phase-field simulations of a series of superlattices with different periodicity. After reproducing the experimental observations, phase-field simulations of  $(\text{PTO})_{10}/(\text{STO})_{10}$  and  $(\text{PTO})_{16}/(\text{STO})_{16}$  superlattices were performed, both of which exhibit vortex lattices. However, in this case, even the introduction of a built-in voltage does not alter the vortex array polarization configurations. Subsequent experimental growth of the corresponding superlattices remarkably confirmed the phase-field predictions on the existence of polar vortices based on the high-resolution polarization mapping [122,123] (Fig. 3).

As shown in Fig. 4, there is a range of superlattice periodicities for which the vortex lattices are predicted to exist by phase-field simulations. The predictions of these different polar states at different periodicity are all confirmed by experimental observations as one can see from the inserts of direct comparisons between phase-field predictions and experimental observations at three different superlattice periodicities. Another advantage of the phase-field method is its capability to provide the full three-dimensional fields of stress and electric fields, polarization, which can then be analyzed to understand the physical mechanisms leading to the formation of

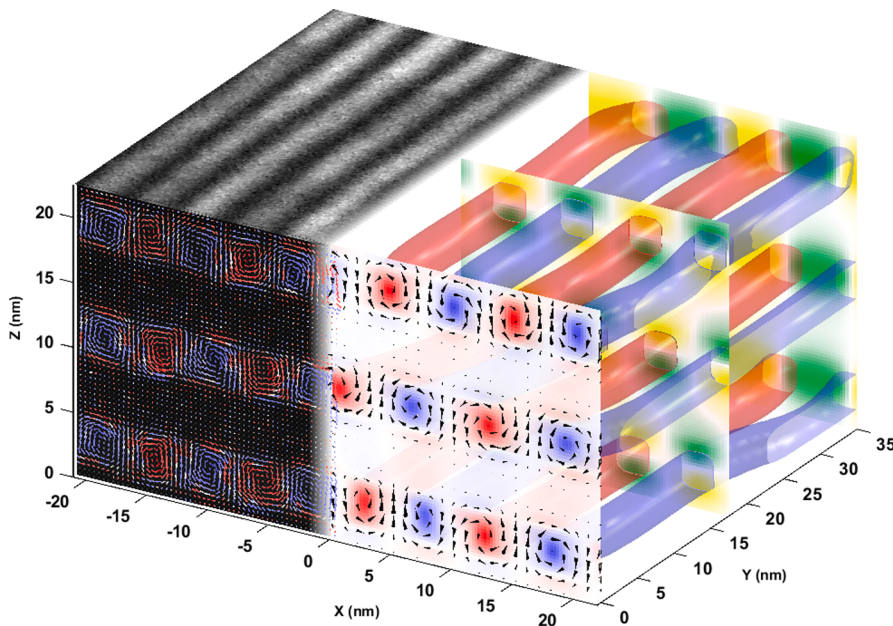


**Fig. 3.** Comparison of experimentally determined and computationally predicted polarization distributions within the PTO layers in a  $(\text{PTO})_{10}/(\text{STO})_{10}$  superlattice. Reprinted (adapted) with permission from [122]. Copyright 2016 Springer Nature.

metastable or stable polar domain states. An analysis of relative energies of different polarization states suggests that their formation and stability are controlled by the competitions among the long-range electrostatic interactions due to the polarization bound charge, long-range elastic interactions arising from the lattice mismatches between the ferroelectric and dielectric layers and between the superlattice film and its substrate, and short-range polarization gradient-related interactions. It is the competition among these interactions that lead to the strong dependence of polarization states as a function of superlattice periodicity from polarization twin domain states, mixed twin/vortex lattice states, vortex lattice, to more conventional domain structures.

One can also employ phase-field simulations to examine the local electrical and mechanical switching of these vortex lattice states, including the possible appearance of transient polar states such as polar skyrmions, wavy polar structures, supercrystals, etc., as well as the existence of an unusual state of negative capacitance. All these predictions have also been confirmed in experiments [124,129,130].

## 12.2. Design of relaxor ferroelectric ceramics with record-high piezoelectricity

This is an example of how an experimentalist, who had no prior experience in computational materials science, was able to learn the phase-field method in a couple of months and employed phase-field simulations to solve a long-standing question with regard to the roles of polar nanoregions in the ultrahigh piezoelectricity of relaxor-ferroelectric solid solution single crystals [131]. He then utilized the fundamental understanding and designed a set of phase-field simulations to guide his own experiments to achieve record-high piezoelectricity in relaxor ferroelectric ceramics [126] as well as in single crystals [127].

Piezoelectric materials, which exhibit electromechanically coupled responses, have been utilized in a wide variety of devices as sensors and transducers. Among known piezoelectrics, a class of perovskite oxide ferroelectrics, called relaxor ferroelectric solid solutions, exhibit the highest piezoelectric coefficient, and hence they are the materials of choice for ultrasonic devices for medical applications, underwater acoustics, and motors.

One of the unique structural features of relaxor-ferroelectric solid solutions is the existence of polar nanoregions that are embedded in normal ferroelectric domains. However, the roles of such polar nanoregions in the piezoelectricity of relaxor ferroelectric crystals is not well understood despite decades of research on this topic. This specific effort starts with quantifying the contribution of polar nanoregions to the dielectric/piezoelectric responses of relaxor-ferroelectric crystals at low temperatures using a combination of experiments and phase-field simulations. Both the phase-field simulations and experimental measurements demonstrate that 50–80% of the room-temperature dielectric and piezoelectric properties come from the polar nanoregions (Fig. 5), confirming our hypothesis that the polar nanoregions have a different polar anisotropy than the matrix [131]. Based on this understanding on the roles of polar nanoregions, a series of phase-field simulations were designed to model the ferroelectric responses of a ferroelectric domain structure with different amounts of polar nanoregions, revealing that the polar nanoregions that exhibit the highest low temperature losses would be the best candidates to enhance the piezoelectricity as they will help the nucleation of new domains and polarization rotation. Based on these simulations, several rare-earth dopants are selected to promote polar nanoregions (Fig. 6). Among them, a small amount of Sm as dopants in  $\text{Pb}(\text{Mg}_{1/3}\text{Nb}_{2/3})\text{O}_3\text{-PbTiO}_3$  (PMN-PT) ceramics leads to an ultrahigh piezoelectric coefficients  $d_{33}$  of as high as 1,500 pC/N and dielectric permittivity  $\epsilon_{33}/\epsilon_0$  larger than 13,000 with a Curie temperature of 89 °C, which is the highest among ceramics [126] (Fig. 7). Very recently, the same strategy was employed in Sm-doped Sm-PMN-PT single crystals to achieve  $d_{33}$  values ranging from 3400 to 4100 pC/N, a record-high value among single crystals [127]. This example offers a successful example of phase-field guided design of dramatically enhanced material properties through the manipulation of the local structural heterogeneity. Such

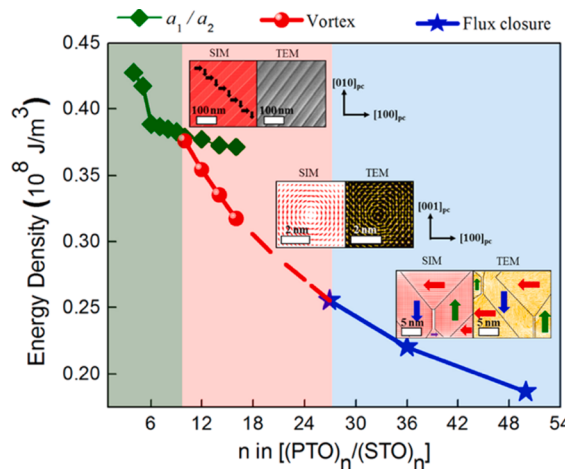


**Fig. 4.** Phase diagram for  $(\text{PTO})_n/(\text{STO})_n$  superlattices on DSO substrate from by phase-field simulations and verified experimentally. Insets: The top shows the simulation and planar TEM result of in-plane view of  $a_1a_2$  twin-domain structure for  $n = 6$ . The middle is the vortex structure for  $n = 10$ . The bottom insets are the cross sections of flux-closure structure for  $n = 50$ . “SIM” and “TEM” stand for simulation and transmission electron microscopy data. Reprinted with permission from [123]. Copyright 2016 American Chemical Society.

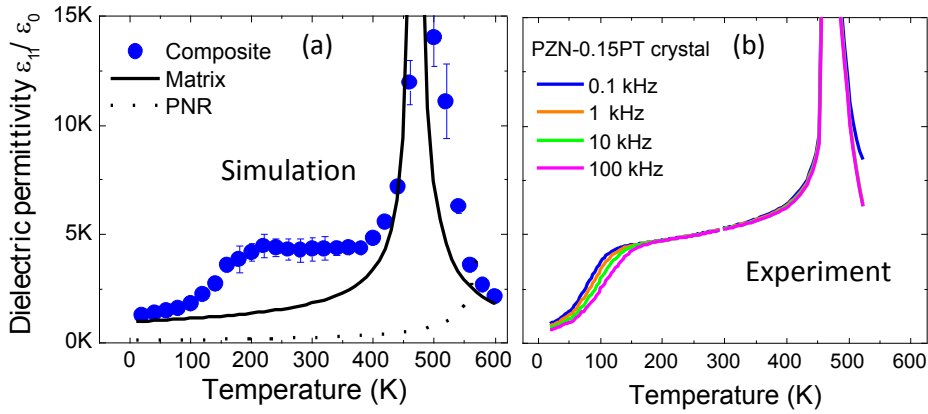


**Fig. 5.** (a) Phase-field simulation of a composite consisting of ferroelectric domains and PNR showing significantly enhanced transverse dielectric permittivity due to the presence of PNR; (b) Experimentally measured results in a PZN-0.15PT crystal confirming the phase-field simulation results. Adapted from [131].

a strategy can be extended to design a wide range of other functional materials such as ferromagnetics, ferroelastics, and ferroic composites.

### 12.3. Discovery of transparent crystals with high piezoelectricity

This is an example on the use of phase-field simulations to discover new functionality of a piezoelectric crystal. Specifically, phase-field simulations of alternative-current (AC) electric field poling of relaxor ferroelectric crystals, combined with the actual crystal growth and characterization, led to the discovery of simultaneous near-perfect light transparency and ultrahigh piezoelectricity in PMN-PT crystals. Such transparent crystals with very high piezoelectricity can potentially be utilized in a wide range of electrically, optically, and mechanically coupled devices from photoacoustic imaging to transparent actuators [128].

PMN-PT relaxor ferroelectric crystals is well known to possess the highest piezoelectricity among piezoelectrics. However, these crystals have always been opaque due to the presence of light-scattering internal domain walls between regions with electric polarization orientated along different directions. In [001]-oriented PMN-PT crystals with rhombohedral symmetry, there are 3 possible types of domain walls, called 71°, 109°, and 180° domain walls, across which the electric polarization directions change by 71, 109, and 180°. In order to be utilized as a piezoelectric, a PMN-PT crystal has to be poled by an electric field to make the crystal macroscopically polar, which essentially eliminates the 180° domain walls. Among the 2 remaining types of domain walls after poling, it can be shown that it is the 71° domain walls that severely scatter light whereas light can transmit across 109° domain walls with little light-scattering. While poling has almost always been performed using direct-current (DC) electric fields, there have been recent experimental evidences that poling using AC electric fields may significantly further increase the piezoelectricity of PMN-PT crystals by another 20–40% [132]. All existing literature attributed this enhanced piezoelectricity of PMN-PT crystals through AC-poling over DC-poling to the increased density of 71° domain walls. However, the phase-field simulations of AC poling of PMN-PT crystals

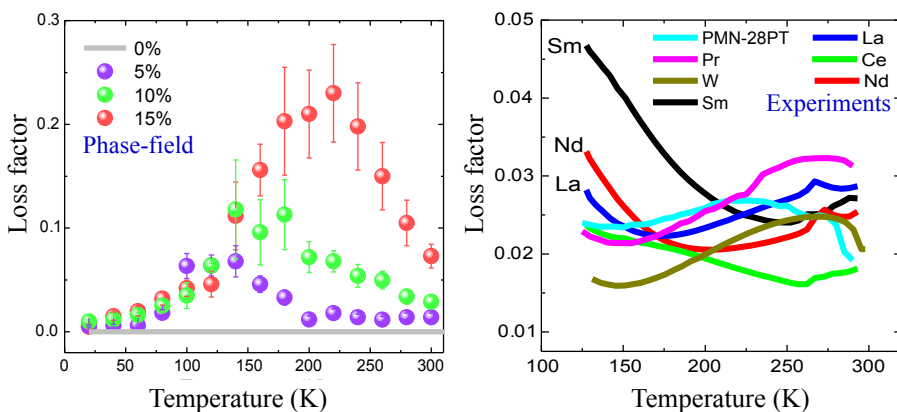


**Fig. 6.** (left) Phase-field simulations demonstrate that a larger volume fraction of heterogeneous regions produces a higher loss maximum; (right) Sm-PMN-PT is selected for further processing and composition optimizations after comparing the measured dielectric losses with the signatures obtained from phase-field simulations. Adapted with permission from [126]. Copyright 2018 Springer Nature.

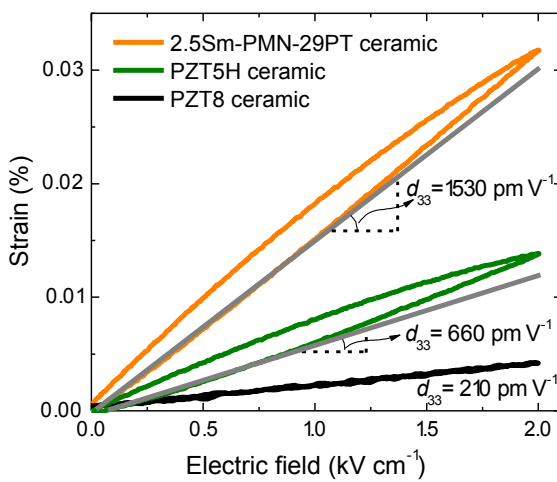


**Fig. 7.** Highly enhanced piezoelectric properties in Sm-PMN-PT. Adapted with permission from [126]. Copyright 2018 Springer Nature.

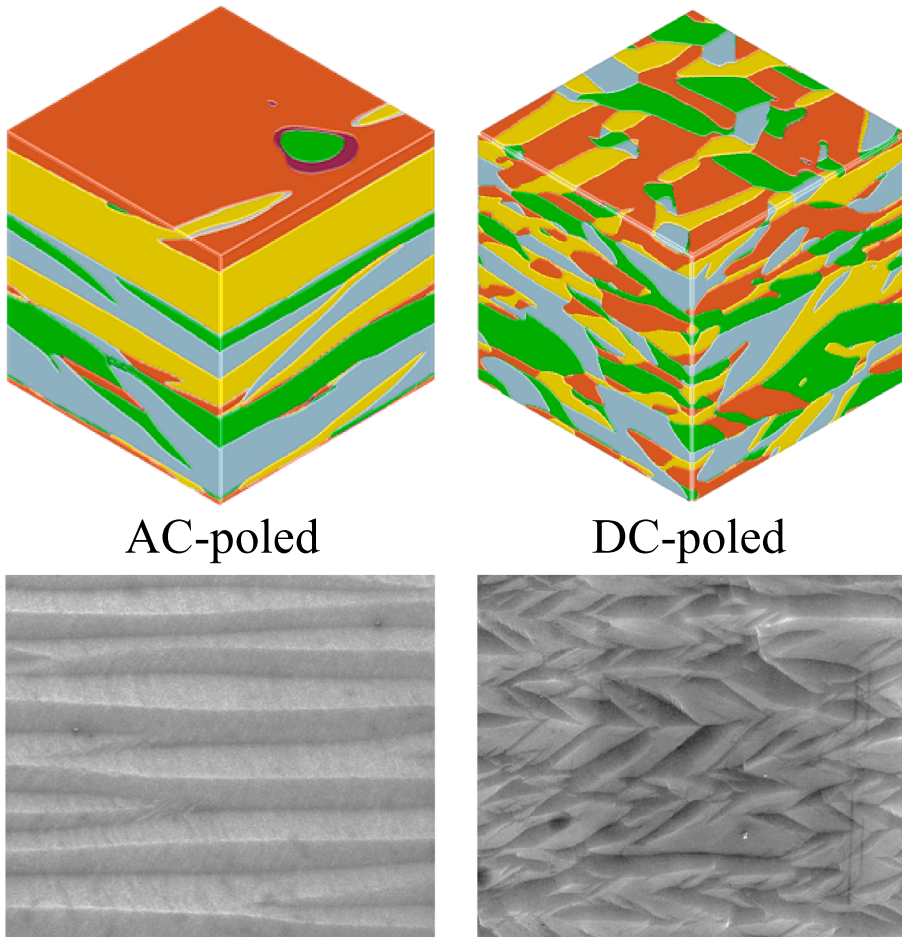


**Fig. 8.** Top row: 3D domain patterns of AC-poled and DC-poled PMN-PT crystals from phase-field simulations (Previously unpublished images, with permission from Bo Wang); bottom row: experimental SEM images of AC-poled and DC-poled patterns showing layer structures along [001] direction (Previously unpublished images, with permission from Fei Li).

demonstrated exactly the opposite, i.e., it drastically reduces the number of light-scattering 71° domain walls, and the 71° domain walls are effectively eliminated after only a few cycles of AC poling (Fig. 8). This is a remarkable and surprising discovery since (a) the observed elimination of 71° domain walls is in direct contradiction with existing literature which claimed to have observed higher domain wall density based solely on surface-sensitive techniques such as piezoresponse force microscopy (PFM); (b) the reduced density of 71° domain walls in PMN-PT can be theoretically rationalized for the improved piezoelectricity by AC-poling over DC-poling, in contrast to the general belief in the community that increasing domain wall density enhances piezoelectricity; and most importantly, (c) the observed elimination of 71° domain walls in the phase-field simulations suggests the enlightening possibility that the AC-poled PMN-PT crystals could be transparent in addition to the enhanced piezoelectricity from AC-poling.

It should be noted here that for bulk single crystals, the domain size obtained from phase-field simulations is typically an order of magnitude smaller than typical microscopic experimental observations. It is computationally challenging to perform phase-field simulations on the scale as large as the crystals used in experiments and at the same time to revolve the polarization/strain profiles across domain walls of the thickness of 1 nm. For example, in Fig. 8, the size of the phase-field simulations is 256 nm while the bottom experimental image is about 10 μm. Therefore, here the sequence of domain evolution predicted by phase-field simulations rather than the actual domain size is critical to providing guidance to experiments.

Guided by phase-field simulations, PMN-PT crystals are experimentally fabricated and are poled using both DC and AC-fields with different frequencies. The bulk characterization techniques such as birefringence imaging microscopy and X-ray diffractions indeed confirmed phase-field predictions that the AC poling cycles successively reduced the number of light-scattering 71° domain walls and almost completely eliminated them after a few AC cycles. Furthermore, by carefully polishing the surface layers and thermal annealing of defects from polishing, PMN-PT crystals are nearly perfectly transparent with improved high piezoelectricity over DC-poled crystals (Fig. 9). It turns out that all existing experimental observation of increased domain wall density through AC-poling was likely due to the fact that all those techniques are only surface-sensitive, i.e., only probing a region within 10 nm from the surface. The breakthrough discovery of simultaneous perfect light transparency and ultrahigh piezoelectricity of relaxor-PT ferroelectric crystals would not be possible without the phase-field simulations.

This work offers an example of theory-guided design of materials to achieve a combination of unprecedented properties and functionalities through domain engineering. The new transparent ferroelectric crystals have a wide range of potential device applications ranging from high-throughput photoacoustic imaging to touch-screen applications.

### 13. A perspective on applications of phase-field method beyond structural alloys

The majority of existing applications of phase-field method are in the area of structural materials, particularly, metallic alloys during solidification, grain growth, and solid-state phase transformations. This will continue to be a major area for applying the phase-field method in the foreseeable future, particularly in modeling microstructure evolution during phase transformations and microstructure evolution in multicomponent alloys such as high entropy alloys [133] or during modern manufacturing processes such as additive manufacturing [134–139]. Another particularly active area of research is developing phase-field models for modeling large deformation of materials and materials failure such as fracture [51,52,140] and dielectric breakdown [141–143]. The present article will emphasize a couple of potential directions to advance the capability of phase-field method in order to expand its applications beyond the conventional processes such as solidification, phase transformations, and microstructure coarsening in metallic alloys.

#### 13.1. Microstructure evolution under highly nonequilibrium conditions

There are materials processes in which a system can be highly out of equilibrium, e.g., under the application of a large and fast external stimulus. Essentially all existing phase-field models, including most of the kinetic equations discussed in this article, are based on linear kinetics, i.e., the rate of change of a phase-field,  $\partial\phi/\partial t$ , is linearly proportional to the driving force for a materials process,

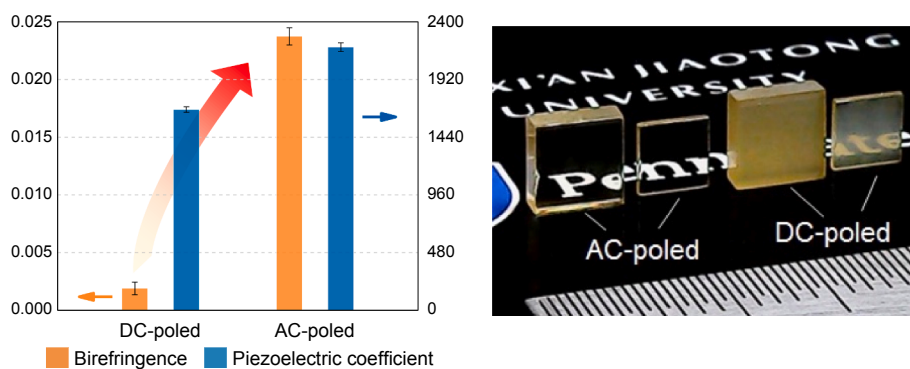


**Fig. 9.** Comparison of Experimentally Measured Properties between AC-poled and Conventional DC-poled [001]-oriented PMN-28PT Crystals. Adapted with permission from [128]. Copyright 2020 Springer Nature.

which is, in principle, only valid for systems that are not too far from equilibrium. For example, mass or heat diffusion flux is assumed to be linearly proportional to the local gradient in chemical potential or temperature. The rate of change of a non-conserved phase-field  $\xi$  is assumed to be linearly proportional to its driving force, or the variational derivative of the total free energy  $F$  with respect to the phase-field variable,  $\delta F/\delta\xi$ . Therefore, existing phase-field models are expected to break down or be inaccurate under conditions of very high electrical, mechanical, or thermal driving forces. There have been recent attempts to extend the capability of current phase-field method to modeling mesoscale materials processes far from equilibrium [144], for example, the dendrite growth at the electrolyte–electrode surface in batteries under a high charging voltage [145]. It is based on the transition state theory which assumes that the rate of a process,  $\partial\xi/\partial t$ , with  $\xi$  representing the extent of the process, is exponentially dependent on the thermodynamic driving force  $A$ , i.e.,

$$\frac{\partial\xi}{\partial t} = L_\xi \left[ \exp\left(\frac{Av}{RT}\right) - 1 \right] = L_\xi^0 \exp\left(-\frac{E_a}{RT}\right) \left[ \exp\left(\frac{Av}{RT}\right) - 1 \right] \quad (13.1)$$

where  $L_\xi$ ,  $L_\xi^0$ , and  $E_a$  are the kinetic rate constant, attempt frequency of a nonequilibrium state to transition to a more stable state, and the energy barrier between initial state and the final state of the process, respectively. In Eq. (13.1),  $A = -\delta F/\delta\xi$  is the thermodynamic driving force in unit of energy per unit volume,  $v$  is the molar volume, and  $R$  is gas constant. At small driving forces, it reduces to the linear kinetics described by the Allen-Cahn equation if the total free energy  $F$  also includes the contribution of the gradient energy in  $\xi$ ,

$$\frac{\partial\xi}{\partial t} = L_\xi \left[ \exp\left(\frac{Av}{RT}\right) - 1 \right] = - \left[ \frac{vL_\xi^0}{RT} \exp\left(-\frac{E_a}{RT}\right) \right] \frac{\delta F}{\delta\xi} \quad (13.2)$$

It remains to be seen if these types of kinetically nonlinear equations can be derived from atomistic theories.

### 13.2. Dynamic phase-field models

In conventional phase-field models, the temporal evolution of mesoscale microstructures is described by relaxational equations that are first order in time, such as the Allen-Cahn (time-dependent Ginzburg-Landau) equation for a non-conserved field and the Cahn-Hilliard equation for a conserved field. Such relaxational and diffusion equations are not sufficient to describe the dynamics of processes and the wave propagation in systems under ultrafast external stimuli. For example, conventional phase-field models for ferroelectric materials employ the relaxational kinetics of polarization evolution as described by the well-known time-dependent Ginzburg-Landau equation while assuming quasistatic elastic equilibrium for the displacement field. There have been existing efforts to include the inertial terms in the phase-field context. As a matter of fact, elastodynamic models have been extensively employed in mechanics of materials to study mechanical wave propagation [146] and implemented in the phase-field model of fracture, see for example references [45,147]. A dynamic phase-field equation was introduced to model the solidification of a pure material [148]. The dynamical equations for both polarization and strain have also recently been introduced into the phase-field model to describe GHz-THz dynamics of ferroelectric and ferroelastic domains under ultrafast stimuli (e.g., laser pulse or electric field pulse), called dynamical phase-field model [149,150]. The model employs the nonlinear Klein-Gordan equation of polarization dynamics [151,152] and the wave equation of elastodynamics, i.e.,

$$\mu_{ij} \frac{\partial^2 P_i}{\partial t^2} + \gamma_{ij} \frac{\partial P_i}{\partial t} + \frac{\delta F}{\delta P_j} = 0 \quad (13.3)$$

$$\rho \frac{\partial^2 u_i}{\partial t^2} = f_{vi} + \frac{\partial}{\partial x_j} \left( \sigma_{ij} + \beta \frac{\partial \sigma_{ij}}{\partial t} \right) \quad (13.4)$$

where  $\mu_{ij}$  and  $\gamma_{ij}$  are effective mass and damping coefficients of the polarization  $P_i$ , respectively and  $F$  is the total free energy. In Eq. (13.4),  $\rho$  is the material density,  $\beta$  is the stiffness damping coefficient, and  $u_i$ ,  $f_{vi}$ , and  $\sigma_{ij}$  are displacements, body force density, and stress fields, respectively.

Such dynamic phase-field models will allow one not only to model the wave propagation in a microstructure but also to extract frequency dependent properties of microstructures.

### 13.3. Coupled structural and electronic phase transitions

A class of materials processes involve coupled processes taking place in electron and lattice systems of the same material. Examples include the coupled electronic and structural/ferroelectric transitions in strongly electron correlated systems such as metal-insulator transitions, superconducting transitions, etc. Due to the nanoscale nature of the structural and electronic patterns, the phase-field method is an ideal approach to modeling and predicting the mesoscale microstructure evolution characterized by the inhomogeneous distributions of structural and electronic order parameters in these materials. For example, Onuki employed a complex order parameter to represent the orbital order during Jahn-Teller structural phase transitions and studied the evolution of the orbital order under an applied uniaxial stress [153]. There have been recent attempts to model the coupled structural and electronic phase transitions, including coupled evolution of free carrier densities, electron correlation order, structural phases, and electric potential [154–158]. For example, it has been used to predict possible emergence of transient electronic phase separation in VO<sub>2</sub> under

photoexcitation [159]. Such models are needed to model and predict rich non-equilibrium lattice and electron dynamics of correlated material systems under ultrafast (GHz-THz optical) stimuli (light, electric field, etc.). Phase-field simulations will be able to provide detailed spatial-temporal description of ultrafast excitation of correlated systems, including each stage of the excitation and relaxation processes with its own characteristic relaxation times.

### 13.4. High throughput phase-field simulations and machine learning

It is now computationally feasible to generate large data sets of realistic 3D microstructures under conditions mimicking experimental synthesis and growth conditions. Therefore, one promising area for the application of phase-field is to combine phase-field simulations, image data construction, and machine learning to optimize microstructures and thus materials properties and performances. The eventual goal should be to provide guidance to experimental synthesis or growth of materials to realize the predictions from a combination of phase-field simulations and machine learning to achieve significantly improved or optimized properties or microstructures with new functionalities, not as mere exercises of practicing machine learning.

To generate microstructure databases for learning demands reliable input thermodynamics and kinetics data. They can be obtained either by fitting to experimental measurements [160] or from databases [161] or a combination of both. There is a need to quantify the uncertainties associated with input parameters and their propagation [162]. A combination of phase-field simulations and machine learning can also be employed to extract materials properties which are otherwise very difficult to compute and experimentally measure. For example, it has been employed to extract the flexoelectric coefficient of a ferroelectric heterostructure [163]. Generating microstructures in a high throughput manner requires efficient numerical algorithms for solving the phase-field equations. One of the options to mitigate the expensive phase-field simulations is to utilize a relatively small sets of phase-field simulation data and use them to develop surrogate models which can generate large amount of data with a moderate computation time [160,164]. Construction of materials microstructure database for learning microstructure-property relations also requires the development of a proper quantitative microstructure representation [165–167].

It is also possible to obtain microstructures and properties directly from phase-field simulations. One can then combine parametric studies using high throughput phase-field simulations and machine learning to provide guidance to experiments. For example, high-throughput phase-field simulations of breakdown strengths were recently performed for the P(VDF-HFP)-based nanocomposites filled with nanoparticles of different properties, and machine learning is conducted on the database from the high-throughput simulations to produce an analytical expression for the breakdown strength of polymer nanocomposites [142,143]. This analytical function is then verified by additional phase-field simulations and targeted experimental measurements. Such theoretical materials design framework can be used to predict the breakdown strength of polymer-based nanocomposites with a wide variety of candidate nanofillers and optimize their energy storage by screening suitable nanofillers. The same strategy can in principle be further extended to design the microstructures and optimize the energy-storage or conversion performances of other materials such as electrode materials of supercapacitors, solid electrolytes, and thermoelectrics.

### Declaration of Competing Interest

The authors declare that they have no known competing financial interests or personal relationships that could have appeared to influence the work reported in this paper.

### Acknowledgments

LQC acknowledges the support from the US Department of Energy, Office of Science, Basic Energy Sciences, under Award Number DE-SC0020145 as part of the Computational Materials Sciences Program and the Hamer Professorship at Penn State from the Donald W. Hamer Foundation.

### References

- [1] Waals JD. Thermodynamique De La Capillarite, Dans L'hypothese D'une Variation Continue De Densite. Archives Neerlandaises 1894;28:121–209.
- [2] Rowlinson JS. Translation of J D Vanderwaals, The Thermodynamic Theory of Capillarity under the Hypothesis of a Continuous Variation of Density. J Stat Phys 1979;20(2):200–44.
- [3] Fix GJ. Phase Field Problems for Free Boundary Problems. In: Free Boundary Problems: Theory and Applications. London: Longman; 1983. p. 580–9.
- [4] Collins JB, Levine H. Diffuse Interface Model of Diffusion-Limited Crystal Growth. Phys Rev B 1985;31(9):6119–22.
- [5] Caginalp G. An Analysis of a Phase Field Model of a Free Boundary. Arch Ration Mech Anal 1986;92(3):205–45.
- [6] Caginalp G, Fife P. Higher-Order Phase Field Models and Detailed Anisotropy. Phys Rev B 1986;34(7):4940–3.
- [7] Wheeler AA, Boettinger WJ, McFadden GB. Phase-Field Model for Isothermal Phase-Transitions in Binary Alloys. Phys Rev A 1992;45(10):7424–39.
- [8] Kobayashi R. Modeling and Numerical Simulations of Dendritic Crystal Growth. Phys D-Nonlin Phenom 1993;63(3–4):410–23.
- [9] Warren JA, Boettinger WJ. Prediction of Dendritic Growth and Microsegregation Patterns in a Binary Alloy Using the Phase-Field Method. Acta Metall Mater 1995;43(2):689–703.
- [10] Karma A, Rappel WJ. Phase-Field Method for Computationally Efficient Modeling of Solidification with Arbitrary Interface Kinetics. Phys Rev E 1996;53(4):R3017–20.
- [11] Karma A, Rappel WJ. Quantitative Phase-Field Modeling of Dendritic Growth in Two and Three Dimensions. Phys Rev E 1998;57(4):4323–49.
- [12] Kim SG, Kim WT, Suzuki T. Interfacial Compositions of Solid and Liquid in a Phase-Field Model with Finite Interface Thickness for Isothermal Solidification in Binary Alloys. Phys Rev E 1998;58(3):3316–23.
- [13] Kim SG, Kim WT, Suzuki T. Phase-Field Model for Binary Alloys. Phys Rev E 1999;60(6):7186–97.

- [14] Beckermann C, Diepers HJ, Steinbach I, Karma A, Tong X. Modeling Melt Convection in Phase-Field Simulations of Solidification. *J Comput Phys* 1999;154(2):468–96.
- [15] Karma A. Phase-Field Formulation for Quantitative Modeling of Alloy Solidification. *Phys Rev Lett* 2001;87(11):115701.
- [16] Echebarria B, Folch R, Karma A, Plapp M. Quantitative Phase-Field Model of Alloy Solidification. *Phys Rev E* 2004;70(6):061604.
- [17] Nestler B, Gärcke H, Stinner B. Multicomponent Alloy Solidification: Phase-Field Modeling and Simulations. *Phys Rev E* 2005;71(4):041609.
- [18] Chen LQ, Yang W. Computer Simulation of the Domain Dynamics of a Quenched System with a Large Number of Nonconserved Order Parameters: The Grain-Growth Kinetics. *Phys Rev B* 1994;50(21):15752–6.
- [19] Steinbach I, Pezzolla F, Nestler B, Seesselberg M, Priele R, Schmitz GJ, et al. A Phase Field Concept for Multiphase Systems. *Phys D-Nonlin Phenom* 1996;94(3):135–47.
- [20] Kobayashi R, Warren JA, Carter WC. A Continuum Model of Grain Boundaries. *Phys D-Nonlin Phenom* 2000;140(1–2):141–50.
- [21] Moelans N, Blanpain B, Wollants P. Quantitative Analysis of Grain Boundary Properties in a Generalized Phase Field Model for Grain Growth in Anisotropic Systems. *Phys Rev B* 2008;78(2):024113.
- [22] Wang Y, Chen LQ, Khachaturyan AG. Kinetics of Strain-Induced Morphological Transformation in Cubic Alloys with a Miscibility Gap. *Acta Metall Mater* 1993;41(1):279–96.
- [23] Zhu JZ, Wang T, Ardell AJ, Zhou SH, Liu ZK, Chen LQ. Three-Dimensional Phase-Field Simulations of Coarsening Kinetics of  $\gamma'$  Particles in Binary Ni-Al Alloys. *Acta Mater* 2004;52(9):2837–45.
- [24] Wang YZ, Wang HY, Chen LQ, Khachaturyan AG. Microstructural Development of Coherent Tetragonal Precipitates in Magnesium-Partially-Stabilized Zirconia - A Computer-Simulation. *J Am Ceram Soc* 1995;78(3):657–61.
- [25] Artemev A, Jin Y, Khachaturyan AG. Three-Dimensional Phase Field Model of Proper Martensitic Transformation. *Acta Mater* 2001;49(7):1165–77.
- [26] Jin YM, Artemev A, Khachaturyan AG. Three-Dimensional Phase Field Model of Low-Symmetry Martensitic Transformation in Polycrystal: Simulation of  $\zeta^2$  Martensite in AuCd Alloys. *Acta Mater* 2001;49(12):2309–20.
- [27] Levitas VI, Preston DL, Lee DW. Three-Dimensional Landau Theory for Multivariant Stress-Induced Martensitic Phase Transformations. III. Alternative Potentials, Critical Nuclei, Kink Solutions, and Dislocation Theory. *Phys Rev B* 2003;68(13):134201.
- [28] Vaithyanathan V, Wolverton C, Chen LQ. Multiscale Modeling of  $\theta'$  Precipitation in Al-Cu Binary Alloys. *Acta Mater* 2004;52(10):2973–87.
- [29] Tang M, Carter WC, Cannon RM. Diffuse Interface Model for Structural Transitions of Grain Boundaries. *Phys Rev B* 2006;73(2):024102.
- [30] Hu HL, Chen LQ. Computer Simulation of Ferroelectric Domain Formation in Two-Dimensions. *Mater Sci Eng A* 1997;A238(1):182–91.
- [31] Li YL, Hu SY, Liu ZK, Chen LQ. Phase-Field Model of Domain Structures in Ferroelectric Thin Films. *Appl Phys Lett* 2001;78(24):3878–80.
- [32] Wang J, Shi SQ, Chen LQ, Li YL, Zhang TY. Phase Field Simulations of Ferroelectric/Ferroelastic Polarization Switching. *Acta Mater* 2004;52(3):749–64.
- [33] Zheng Y, Wang B, Woo CH. Simulation of Interface Dislocations Effect on Polarization Distribution of Ferroelectric Thin Films. *Appl Phys Lett* 2006;88(9):092903.
- [34] Su Y, Landis CM. Continuum Thermodynamics of Ferroelectric Domain Evolution: Theory, Finite Element Implementation, and Application to Domain Wall Pinning. *J Mech Phys Solids* 2007;55(2):280–305.
- [35] Schrade D, Mueller R, Xu BX, Gross D. Domain Evolution in Ferroelectric Materials: A Continuum Phase Field Model and Finite Element Implementation. *Comput Meth Appl Mech Eng* 2007;196(41–44):4365–74.
- [36] Guyer JE, Boettger WJ, Warren JA, McFadden GB. Phase Field Modeling of Electrochemistry. I. Equilibrium. *Phys Rev E* 2004;69(2):021603.
- [37] Han BC, Van der Ven A, Morgan D, Ceder G. Electrochemical Modeling of Intercalation Processes with Phase Field Models. *Electrochim Acta* 2004;49(26):4691–9.
- [38] Cogswell DA, Bazant MZ. Coherency Strain and the Kinetics of Phase Separation in LiFePO<sub>4</sub> Nanoparticles. *ACS Nano* 2012;6(3):2215–25.
- [39] Hong L, Yang KQ, Tang M. A Mechanism of Defect-Enhanced Phase Transformation Kinetics in Lithium Iron Phosphate Olivine. *npj Comput Mater* 2019;5(118):1–9.
- [40] Wang YU, Jin YM, Cuitino AM, Khachaturyan AG. Nanoscale Phase Field Microelasticity Theory of Dislocations: Model and 3D Simulations. *Acta Mater* 2001;49(10):1847–57.
- [41] Rodney D, Le Bouar Y, Finel A. Phase Field Methods and Dislocations. *Acta Mater* 2003;51(1):17–30.
- [42] Shen C, Wang Y. Incorporation of  $\gamma$ -Surface to Phase Field Model of Dislocations: Simulating Dislocation Dissociation in Fcc Crystals. *Acta Mater* 2004;52(3):683–91.
- [43] Clayton JD, Knap J. A Phase Field Model of Deformation Twinning: Nonlinear Theory and Numerical Simulations. *Phys D-Nonlin Phenom* 2011;240(9–10):841–58.
- [44] Heo TW, Wang Y, Bhattacharya S, Sun X, Hu SY, Chen LQ. A Phase-Field Model for Deformation Twinning. *Philos Mag Lett* 2011;91(2):110–21.
- [45] Karma A, Kessler DA, Levine H. Phase-Field Model of Mode III Dynamic Fracture. *Phys Rev Lett* 2001;87(4):045501.
- [46] Kuhn C, Müller R. A Continuum Phase Field Model for Fracture. *Eng Fract Mech* 2010;77(18):3625–34.
- [47] Miehe C, Hofacker M, Welschinger F. A Phase Field Model for Rate-Independent Crack Propagation: Robust Algorithmic Implementation Based on Operator Splits. *Comput Meth Appl Mech Eng* 2010;199(45–48):2765–78.
- [48] Borden MJ, Verhoosel CV, Scott MA, Hughes TJR, Landis CM. A Phase-Field Description of Dynamic Brittle Fracture. *Comput Meth Appl Mech Eng* 2012;217–220:77–95.
- [49] Borden MJ, Hughes TJR, Landis CM, Verhoosel CV. A Higher-Order Phase-Field Model for Brittle Fracture: Formulation and Analysis within the Isogeometric Analysis Framework. *Comput Meth Appl Mech Eng* 2014;273:100–18.
- [50] Ambati M, Gerasimov T, De Lorenzis L. Phase-Field Modeling of Ductile Fracture. *Comput Mech* 2015;55(5):1017–40.
- [51] Wu JY. A Unified Phase-Field Theory for the Mechanics of Damage and Quasi-Brittle Failure. *J Mech Phys Solids* 2017;103:72–99.
- [52] Mesgarnejad A, Karma A. Vulnerable Window of Yield Strength for Swelling-Driven Fracture of Phase-Transforming Battery Materials. *npj Comput Mater* 2020;6(58):1–10.
- [53] Du Q, Liu C, Wang XQ. A Phase Field Approach in the Numerical Study of the Elastic Bending Energy for Vesicle Membranes. *J Comput Phys* 2004;198(2):450–68.
- [54] Lowengrub JS, Ratz A, Voigt A. Phase-Field Modeling of the Dynamics of Multicomponent Vesicles: Spinodal Decomposition, Coarsening, Budding, and Fission. *Phys Rev E* 2009;79(3):031926.
- [55] Shao DY, Rappel WJ, Levine H. Computational Model for Cell Morphodynamics. *Phys Rev Lett* 2010;105(10):108104.
- [56] Zieber F, Aranson IS. Computational Approaches to Substrate-Based Cell Motility. *npj Comput Mater* 2016;2(16019):1–16.
- [57] Sigmund O, Maute K. Topology Optimization Approaches a Comparative Review. *Struct Multidiscip Optim* 2013;48(6):1031–55.
- [58] Preusser T, Droske M, Garbe CS, Telea A, Rumpf M. A Phase Field Method for Joint Denoising, Edge Detection, and Motion Estimation in Image Sequence Processing. *SIAM J Appl Math* 2007;68(3):599–618.
- [59] Bertozzi AL, Flenner A. Diffuse Interface Models on Graphs for Classification of High Dimensional Data. *Multiscale Model Simul* 2012;10(3):1090–118.
- [60] Bertozzi AL, Flenner A. Diffuse Interface Models on Graphs for Classification of High Dimensional Data. *SIAM Rev* 2016;58(2):293–328.
- [61] Antil H, Bartels S. Spectral Approximation of Fractional PDEs in Image Processing and Phase Field Modeling. *Comput Meth Appl Math* 2017;17(4):661–78.
- [62] Chen LQ. Phase-Field Models for Microstructure Evolution. *Annu Rev Mater Res* 2002;32(1):113–40.
- [63] Emmerich H. Advances of and by Phase-Field Modelling in Condensed-Matter Physics. *Adv Phys* 2008;57(1):1–87.
- [64] Moelans N, Blanpain B, Wollants P. An Introduction to Phase-Field Modeling of Microstructure Evolution. *Comp Coupl Phase Diagr Thermochem* 2008;32(2):268–94.
- [65] Singer-Loginova I, Singer HM. The Phase Field Technique for Modeling Multiphase Materials. *Rep Prog Phys* 2008;71(10):106501.
- [66] Steinbach I. Phase-Field Models in Materials Science. *Modell Simul Mater Sci Eng* 2009;17(7):073001.
- [67] Wang YZ, Li J. Phase Field Modeling of Defects and Deformation. *Acta Mater* 2010;58(4):1212–35.
- [68] Steinbach I. Phase-Field Model for Microstructure Evolution at the Mesoscopic Scale. *Annu Rev Mater Res* 2013;43:89–107.

- [69] Tonks MR, Aagesen LK. The Phase Field Method: Mesoscale Simulation Aiding Material Discovery. *Annu Rev Mater Res* 2019;49:79–102.
- [70] Boettinger WJ, Warren JA, Beckermann C, Karma A. Phase-Field Simulation of Solidification. *Annu Rev Mater Res* 2002;32(1):163–94.
- [71] Thornton K, Agren J, Voorhees PW. Modelling the Evolution of Phase Boundaries in Solids at the Meso- and Nano-Scales. *Acta Mater* 2003;51(19):5675–710.
- [72] Militzer M. Phase Field Modeling of Microstructure Evolution in Steels. *Curr Opin Solid State Mater Sci* 2011;15(3):106–15.
- [73] Mamivand M, Zaeem MA, El Kadiri H. A Review on Phase Field Modeling of Martensitic Phase Transformation. *Comput Mater Sci* 2013;77:304–11.
- [74] Chen LQ. Phase-Field Method of Phase Transitions/Domain Structures in Ferroelectric Thin Films: A Review. *J Am Ceram Soc* 2008;91(6):1835–44.
- [75] Wang JJ, Wang B, Chen LQ. Understanding, Predicting, and Designing Ferroelectric Domain Structures and Switching Guided by the Phase-Field Method. *Annu Rev Mater Res* 2019;49:127–52.
- [76] Clayton JD. Mesoscale Models of Interface Mechanics in Crystalline Solids: A Review. *J Mater Sci* 2018;53(8):5515–45.
- [77] Granasy L, Toth GI, Warren JA, Podmaniczky F, Tegze G, Ratkai L, et al. Phase-Field Modeling of Crystal Nucleation in Undercooled Liquids - A Review. *Prog Mater Sci* 2019;106:100569.
- [78] Devanathan R, Van Brusel L, Chartier A, Gueneau C, Mattsson AE, Tikare V, et al. Modeling and Simulation of Nuclear Fuel Materials. *Energy Environ Sci* 2010;3(10):1406–26.
- [79] Millett PC, Tonks M. Application of Phase-Field Modeling to Irradiation Effects in Materials. *Curr Opin Solid State Mater Sci* 2011;15(3):125–33.
- [80] Li YL, Hu SY, Sun X, Stan M, Review A. Applications of the Phase Field Method in Predicting Microstructure and Property Evolution of Irradiated Nuclear Materials. *npj Comput Mater* 2017;3(16):1–17.
- [81] Wang Q, Zhang G, Li YJ, Hong ZJ, Wang D, Shi SQ. Application of Phase-Field Method in Rechargeable Batteries. *npj Comput Mater* 2020;6(176):1–8.
- [82] Momeni K, Ji YZ, Wang YX, Paul S, Neshani S, Yilmaz DE, et al. Multiscale Computational Understanding and Growth of 2D Materials: A Review. *npj Comput Mater* 2020;6(22):1–18.
- [83] Anderson DM, McFadden GB, Wheeler AA. Diffuse-Interface Methods in Fluid Mechanics. *Annu Rev Fluid Mech* 1998;30(1):139–65.
- [84] Jacqmin D. Calculation of Two-Phase Navier-Stokes Flows Using Phase-Field Modeling. *J Comput Phys* 1999;155(1):96–127.
- [85] Kim J. Phase-Field Models for Multi-Component Fluid Flows. *Comm Comput Phys* 2012;12(3):613–61.
- [86] Elder KR, Katakowski M, Haataja M, Grant M. Modeling Elasticity in Crystal Growth. *Phys Rev Lett* 2002;88(24):245701.
- [87] Emmerich H, Lowen H, Wittkowski R, Gruhn T, Toth GI, Tegze G, et al. Phase-Field-Crystal Models for Condensed Matter Dynamics on Atomic Length and Diffusive Time Scales: An Overview. *Adv Phys* 2012;61(6):665–743.
- [88] Khachaturyan AG. Microscopic Theory of Diffusion in Crystalline Solid Solutions and Time Evolution of Diffuse Scattering of X-Rays and Thermal Neutrons. *Soviet Physics Solid State*, Ussr 1968;9(9):2040.
- [89] Khachaturyan AG. Theory of Structural Transformations in Solids. New York: John Wiley and Sons; 1983.
- [90] Chen LQ, Khachaturyan AG. Computer Simulation of Structural Transformations During Precipitation of an Ordered Intermetallic Phase. *Acta Metall Mater* 1991;39(11):2533–51.
- [91] Penrose O, Fife PC. Thermodynamically Consistent Models of Phase-Field Type for the Kinetics of Phase Transitions. *Phys D-Nonlin Phenom* 1990;43(1):44–62.
- [92] Wang SL, Sekerka RF, Wheeler AA, Murray BT, Coriell SR, Braun RJ, et al. Thermodynamically-Consistent Phase-Field Models for Solidification. *Phys D-Nonlin Phenom* 1993;69(1–2):189–200.
- [93] Fried E, Gurtin ME. Continuum Theory of Thermally Induced Phase Transitions Based on an Order Parameter. *Phys D-Nonlin Phenom* 1993;68(3–4):326–43.
- [94] Gurtin ME. Generalized Ginzburg-Landau and Cahn-Hilliard Equations Based on a Microforce Balance. *Phys D-Nonlin Phenom* 1996;92(3–4):178–92.
- [95] Cahn JW. On Spinodal Decomposition. *Acta Metall* 1961;9(9):795–801.
- [96] Allen SM, Cahn JW. A Microscopic Theory for Antiphase Boundary Motion and Its Application to Antiphase Domain Coarsening. *Acta Metall* 1979;27(6):1085–95.
- [97] Devonshire AF. Theory of Ferroelectrics. *Adv Phys* 1954;3(10):85–130.
- [98] Chen LQ, Wang YZ, Khachaturyan AG. Transformation-Induced Elastic Strain Effect on the Precipitation Kinetics of Ordered Intermetallics. *Philos Mag Lett* 1991;64(5):241–51.
- [99] Koyama T, Miyazaki T, Mebed A. Computer Simulations of Phase Decomposition in Real Alloy Systems Based on the Modified Khachaturyan Diffusion Equation. *Metall Mater Trans A* 1995;26(10):2617–23.
- [100] Semenovskaya S, Khachaturyan AG. Structural Transformations in Nonstoichiometric  $\text{YBa}_2\text{Cu}_3\text{O}_{6+\delta}$ . *Phys Rev B* 1992;46(10):6511–34.
- [101] Wang YZ, Chen LQ, Khachaturyan AG. Shape Evolution of a Precipitate During Strain-Induced Coarsening - A Computer Simulation. *Scr Metall Mater* 1991;25(6):1387–92.
- [102] Yang YB, Zhao YH, Tian XL, Hou H. Microscopic Phase-Field Simulation for Precipitation Process of  $\text{Ni}_60\text{Al}_{20}\text{V}_{20}$  Medium Entropy Alloy. *Acta Physica Sinica* 2020;69(14):140201.
- [103] Chen LQ. Kinetics of Ordering and Spinodal Decomposition in the Pair Approximation. *Phys Rev B* 1998;58(9):5266–74.
- [104] Martin G. Relaxation Rate of Conserved and Nonconserved Order Parameters in Replacive Transitions. *Phys Rev B* 1994;50(17):12362–6.
- [105] Le Bouar Y, Khachaturyan AG. Mechanism and Modeling of Saw-Tooth Structure Formation in the  $\text{L}1_2$ - $\text{L}1_0$  Two-Phase System. *Acta Mater* 2000;48(8):1705–17.
- [106] Chen LQ, Wang YZ, Khachaturyan AG. Kinetics of Tweed and Twin Formation During an Ordering Transition in a Substitutional Solid Solution. *Philos Mag Lett* 1992;65(1):15–23.
- [107] Chen LQ, Khachaturyan AG. Dynamics of Simultaneous Ordering and Phase Separation and Effect of Long Range Coulomb Interactions. *Phys Rev Lett* 1993;70(10):1477–80.
- [108] Elder KR, Huang ZF, Provatas N. Amplitude Expansion of the Binary Phase-Field-Crystal Model. *Phys Rev E* 2010;81(1):011602.
- [109] Goldenfeld N, Athreya BP, Dantzig JA. Renormalization Group Approach to Multiscale Simulation of Polycrystalline Materials Using the Phase Field Crystal Model. *Phys Rev E* 2005;72(2):020601(R).
- [110] Jin YM, Khachaturyan AG. Atomic Density Function Theory and Modeling of Microstructure Evolution at the Atomic Scale. *J Appl Phys* 2006;100(1):013519.
- [111] Greenwood M, Provatas N, Rottler J. Free Energy Functionals for Efficient Phase Field Crystal Modeling of Structural Phase Transformations. *Phys Rev Lett* 2010;105(4):045702.
- [112] Wu KA, Adland A, Karma A. Phase-Field-Crystal Model for Fcc Ordering. *Phys Rev E* 2010;81(6):061601.
- [113] Greenwood M, Rottler J, Provatas N. Phase-Field-Crystal Methodology for Modeling of Structural Transformations. *Phys Rev E* 2011;83(3):031601.
- [114] Granasy L, Podmaniczky F, Toth GI, Tegze G, Puszta T. Heterogeneous Nucleation of/on Nanoparticles: A Density Functional Study Using the Phase- Field Crystal Model. *Chem Soc Rev* 2014;43(7):2159–73.
- [115] Asadi E, Zaeem MA. A Review of Quantitative Phase-Field Crystal Modeling of Solid-Liquid Structures. *Jom* 2015;67(1):186–201.
- [116] Tagantsev AK. The Role of the Background Dielectric Susceptibility in Uniaxial Ferroelectrics. *Ferroelectrics* 1986;69(1):321–3.
- [117] Tagantsev AK. Landau Expansion for Ferroelectrics: Which Variable to Use? *Ferroelectrics* 2008;375(1):19–27.
- [118] Woo CH, Zheng Y. Depolarization in Modeling Nano-Scale Ferroelectrics Using the Landau Free Energy Functional. *Appl Phys a-Mater Sci Process* 2008;91(1):59–63.
- [119] Levanyuk AP, Strukov BA, Cano A. Background Dielectric Permittivity: Material Constant or Fitting Parameter? *Ferroelectrics* 2016;503(1):94–103.
- [120] Wang JJ, Ma XQ, Li Q, Britton J, Chen LQ. Phase Transitions and Domain Structures of Ferroelectric Nanoparticles: Phase Field Model Incorporating Strong Elastic and Dielectric Inhomogeneity. *Acta Mater* 2013;61(20):7591–603.
- [121] Zhang JX, Chen LQ. Phase-Field Microelasticity Theory and Micromagnetic Simulations of Domain Structures in Giant Magnetostrictive Materials. *Acta Mater* 2005;53(9):2845–55.
- [122] Yadav AK, Nelson CT, Hsu SL, Hong Z, Clarkson JD, Schlepütz CM, et al. Observation of Polar Vortices in Oxide Superlattices. *Nature* 2016;530(7589):198–201.

- [123] Hong ZJ, Damodaran AR, Xue F, Hsu SL, Britson J, Yadav AK, et al. Stability of Polar Vortex Lattice in Ferroelectric Superlattices. *Nano Lett* 2017;17(4):2246–52.
- [124] Das S, Tang YL, Hong Z, Goncalves MAP, McCarter MR, Klewe C, et al. Observation of Room-Temperature Polar Skyrmiions. *Nature* 2019;568(7752):368–72.
- [125] Yadav AK, Nguyen KX, Hong ZJ, Garcia-Fernandez P, Aguado-Puente P, Nelson CT, et al. Spatially Resolved Steady-State Negative Capacitance. *Nature* 2019;565(7740):468–71.
- [126] Li F, Lin DB, Chen ZB, Cheng ZX, Wang JL, Li CC, et al. Ultrahigh Piezoelectricity in Ferroelectric Ceramics by Design. *Nat Mater* 2018;17(4):349–54.
- [127] Li F, Cabral MJ, Xu B, Cheng ZX, Dickey EC, LeBeau JM, et al. Giant Piezoelectricity of Sm-Doped Pb(Mg<sub>1/3</sub>Nb<sub>2/3</sub>)O<sub>3</sub>-PbTiO<sub>3</sub> Single Crystals. *Science* 2019;364(6437):264–8.
- [128] Qiu CR, Wang B, Zhang N, Zhang SJ, Liu JF, Walker D, et al. Transparent Ferroelectric Crystals with Ultrahigh Piezoelectricity. *Nature* 2020;577(7790):350–4.
- [129] Damodaran AR, Clarkson JD, Hong Z, Liu H, Yadav AK, Nelson CT, et al. Phase Coexistence and Electric-Field Control of Toroidal Order in Oxide Superlattices. *Nat Mater* 2017;16(10):1003–9.
- [130] Stoica VA, Laanait N, Dai C, Hong Z, Yuan Y, Zhang Z, et al. Optical Creation of a Supercrystal with Three-Dimensional Nanoscale Periodicity. *Nat Mater* 2019;18(4):377–83.
- [131] Li F, Zhang SJ, Yang TN, Xu Z, Zhang N, Liu G, et al. The Origin of Ultrahigh Piezoelectricity in Relaxor-Ferroelectric Solid Solution Crystals. *Nat Commun* 2016;7(13807):1–9.
- [132] Jiao ZQ, Chen LQ, Xia LJ, Yang YY, Zheng Y, Chen HX, et al. Harnessing Multiplex Polymerase Chain Reaction Assay for Convenient and Simultaneous Differentiation of Testudinins Carapax Et Plastrum from Trionycis Carapax. *Pharmacogn Mag* 2020;16(69):393–9.
- [133] Li JL, Li Z, Wang Q, Dong C, Liaw PK. Phase-Field Simulation of Coherent BCC/B2 Microstructures in High Entropy Alloys. *Acta Mater* 2020;197:10–9.
- [134] Gong XB, Chou K. Phase-Field Modeling of Microstructure Evolution in Electron Beam Additive Manufacturing. *Jom* 2015;67(5):1176–82.
- [135] Keller T, Lindwall G, Ghosh S, Ma L, Lane BM, Zhang F, et al. Application of Finite Element, Phase-Field, and CALPHAD-Based Methods to Additive Manufacturing of Ni-Based Superalloys. *Acta Mater* 2017;139:244–53.
- [136] Ji YZ, Chen L, Chen LQ. Understanding Microstructure Evolution During Additive Manufacturing of Metallic Alloys Using Phase-Field Modeling. In Gouge M, Michaleris P, editors, Thermo-Mechanical Modeling of Additive Manufacturing; 2018, p. 93–116.
- [137] Liu PW, Ji YZ, Wang Z, Qiu CL, Antonysamy AA, Chen LQ, et al. Investigation on Evolution Mechanisms of Site-Specific Grain Structures During Metal Additive Manufacturing. *J Mater Process Technol* 2018;257:191–202.
- [138] Lu LX, Sridhar N, Zhang YW. Phase Field Simulation of Powder Bed-Based Additive Manufacturing. *Acta Mater* 2018;144:801–9.
- [139] Yang YYW, Ragnvaldsen O, Bai Y, Yi M, Xu BX. 3D Non-Isothermal Phase-Field Simulation of Microstructure Evolution During Selective Laser Sintering. *npj Comput Mater* 2019;5(81):1–12.
- [140] Clayton JD, Knap J. Phase Field Modeling and Simulation of Coupled Fracture and Twinning in Single Crystals and Polycrystals. *Comput Meth Appl Mech Eng* 2016;312:447–67.
- [141] Pitike KC, Hong W. Phase-Field Model for Dielectric Breakdown in Solids. *J Appl Phys* 2014;115(4):044101.
- [142] Shen ZH, Wang JJ, Lin YH, Nan CW, Chen LQ, Shen Y. High-Throughput Phase-Field Design of High-Energy-Density Polymer Nanocomposites. *Adv Mater* 2018;30(2):1704380.
- [143] Shen ZH, Wang JJ, Jiang JY, Huang SX, Lin YH, Nan CW, et al. Phase-Field Modeling and Machine Learning of Electric-Thermal-Mechanical Breakdown of Polymer-Based Dielectrics. *Nat Commun* 2018;9(10):1–10.
- [144] Liang LY, Qi Y, Xue F, Bhattacharya S, Harris SJ, Chen LQ. Nonlinear Phase-Field Model for Electrode-Electrolyte Interface Evolution. *Phys Rev E* 2012;86(5):051609.
- [145] Chen L, Zhang HW, Liang LY, Liu Z, Qi Y, Lu P, et al. Modulation of Dendritic Patterns During Electrodeposition: A Nonlinear Phase-Field Model. *J Power Sources* 2015;300:376–85.
- [146] Milton GW, Willis JR. On Modifications of Newton's Second Law and Linear Continuum Elastodynamics. *Proc Roy Soc a-Math Phys Eng Sci* 2007;463(2079):855–80.
- [147] Tian FC, Zeng J, Tang XL, Xu TY, Li LB. A Dynamic Phase Field Model with No Attenuation of Wave Speed for Rapid Fracture Instability in Hyperelastic Materials. *Int J Solids Struct* 2020;202:685–98.
- [148] Salhoumi A, Galenko PK. Fast Traveling Waves in the Phase-Field Theory: Effective Mobility Approach Versus Kinetic Energy Approach. *J Phys: Condens Matter* 2020;32(20):204003.
- [149] Akamatsu H, Yuan YK, Stoica VA, Stone G, Yang TN, Hong ZJ, et al. Light-Activated Gigahertz Ferroelectric Domain Dynamics. *Phys Rev Lett* 2018;120(9):096101.
- [150] Yang TN, Wang B, Hu JM, Chen LQ. Domain Dynamics under Ultrafast Electric-Field Pulses. *Phys Rev Lett* 2020;124(10):107601.
- [151] Glinchuk MD, Eliseev EA, Stephanovich VA. Dynamical Dielectric Susceptibility of Ferroelectric Thin Films and Multilayers. *Phys Solid State* 2002;44(5):911–22.
- [152] Bandyopadhyay AK, Ray PC, Gopalan V. An Approach to the Klein-Gordon Equation for a Dynamic Study in Ferroelectric Materials. *J Phys-Conden Matter* 2006;18(16):4093–9.
- [153] Onuki A. Ginzburg-Landau Theory of Jahn-Teller Phase Transitions. *J Phys Soc Jpn* 2001;70(12):3479–82.
- [154] Yusupov R, Mertelj T, Kabanov VV, Brazovskii S, Kusar P, Chu JH, et al. Coherent Dynamics of Macroscopic Electronic Order through a Symmetry Breaking Transition. *Nat Phys* 2010;6(9):681–4.
- [155] Shi Y, Xue F, Chen LQ. Ginzburg-Landau Theory of Metal-Insulator Transition in VO<sub>2</sub>: The Electronic Degrees of Freedom. *EPL* 2017;120(4):46003.
- [156] Tagaras MR, Weng J, Allen RE. Time-Dependent Ginzburg-Landau Model for Light-Induced Superconductivity in the Cuprate LSCO. *Eur Phys J-Spec Top* 2019;227(15–16):2297–301.
- [157] Dolgirev PE, Rozhkov AV, Zong A, Kogar A, Gedik N, Fine BV. Amplitude Dynamics of the Charge Density Wave in LaTe<sub>3</sub>: Theoretical Description of Pump-Probe Experiments. *Phys Rev B* 2020;101(5):054203.
- [158] Sun ZY, Millis AJ. Transient Trapping into Metastable States in Systems with Competing Orders. *Phys Rev X* 2020;10(2):021028.
- [159] Shi Y, Chen LQ. Spinodal Electronic Phase Separation During Insulator-Metal Transitions. *Phys Rev B* 2020;102(19):195101.
- [160] Wang Z, Liu PW, Ji YZ, Mahadevan S, Horstemeyer MF, Hu Z, et al. Uncertainty Quantification in Metallic Additive Manufacturing through Physics-Informed Data-Driven Modeling. *Jom* 2019;71(8):2625–34.
- [161] Zhang J, Poulsen SO, Gibbs JW, Voorhees PW, Poulsen HF. Determining Material Parameters Using Phase-Field Simulations and Experiments. *Acta Mater* 2017;129:229–38.
- [162] Attari V, Honarmandi P, Duong T, Sauceda DJ, Allaire D, Arroyave R. Uncertainty Propagation in a Multiscale CALPHAD-Reinforced Elastochemical Phase-Field Model. *Acta Mater* 2020;183:452–70.
- [163] Li Q, Nelson CT, Hsu S-L, Damodaran AR, Li L-L, Yadav AK, et al. Quantification of Flexoelectricity in PbTiO<sub>3</sub>/SrTiO<sub>3</sub> Superlattice Polar Vortices Using Machine Learning and Phase-Field Modeling. *Nat Commun* 2017;8(1468):1–8.
- [164] Wang Z, Liu PW, Xiao YH, Cui XY, Hui Z, Chen L. A Data-Driven Approach for Process Optimization of Metallic Additive Manufacturing under Uncertainty. *J Manuf Sci Eng-Trans Asme* 2019;141(8):081004.
- [165] DeCost BL, Holm EA. A Computer Vision Approach for Automated Analysis and Classification of Microstructural Image Data. *Comput Mater Sci* 2015;110:126–33.
- [166] Steinmetz P, Yabansu YC, Hotzer J, Jaintia M, Nestler B, Kalidindi SR. Analytics for Microstructure Datasets Produced by Phase-Field Simulations. *Acta Mater* 2016;103:192–203.
- [167] Yabansu YC, Steinmetz P, Hotzer J, Kalidindi SR, Nestler B. Extraction of Reduced-Order Process-Structure Linkages from Phase-Field Simulations. *Acta Mater* 2017;124:182–94.